

Active Galactic Nuclei and STaR fOrmation in Nearby Galaxies (AGNSTRONG). III. A Study on Ionized and Warm Molecular Gas Outflows of 6 Type-2 AGNs

RUISONG XIA,^{1,2} CHEN QIN,^{1,2} HUYNH ANH N. LE^{✉,1,2} YONGQUAN XUE^{✉,1,2} SHIFU ZHU,^{1,2} MENGQIU HUANG,^{1,2} HAO LIU,^{1,2} AND XIAOZHI LIN^{1,2}

¹Department of Astronomy, University of Science and Technology of China, Hefei 230026, China; lha@ustc.edu.cn, xuey@ustc.edu.cn

²School of Astronomy and Space Science, University of Science and Technology of China, Hefei 230026, China

ABSTRACT

Active galactic nucleus (AGN)-driven gas outflows are one of the best tracers of AGN feedback in action, as these powerful outflows expel/heat or compress the surrounding interstellar medium (ISM), thus quenching or enhancing star-forming activity in their hosts. Studying the kinematics of outflows in different gas phases is crucial for comprehending how AGNs impact the ISM within their host galaxies. However, the differences in the physical natures of ionized and warm molecular gas outflows remain largely unexplored. To obtain a complete picture of AGN outflows and their feedback effects, we present a study of both ionized and warm molecular gas outflows in six type-2 AGNs ($z < 0.1$) that exhibit strong ionized outflows in previous optical observations. Utilizing the Triple Spectrograph and Double Spectrograph instruments on the Palomar 200-inch Hale Telescope, we conduct spatially resolved measurements in the slit direction of strong emission lines from both ionized and warm molecular gas, such as [O III], Pa α , H $_2$ 1-0 S(1), etc., allowing for a direct comparison of their outflow properties. One out of six AGNs shows significant ionized and warm molecular outflows in near-infrared bands, exhibiting the most powerful kinematics and highest luminosity. A positive correlation between the kinematics and AGN luminosity is shown, suggesting that more luminous AGNs, which reflect higher levels of AGN activity, tend to have a greater impact on the gases, probably driving the outflows.

Keywords: galaxies: active - galaxies: kinematics

1. INTRODUCTION

The correlations between the mass of the central supermassive black hole (SMBH) and the properties of the host galaxy hint at a co-evolution of black holes (BHs) and galaxies, which may be regulated by active galactic nucleus (AGN) feedback (e.g., Kormendy & Ho 2013; Xue 2017; Caglar et al. 2020), as predicted by theoretical studies. The two primary scenarios, negative and positive feedback, are employed to interpret the observed results (e.g., Zubovas & King 2014; Le et al. 2017a,b; Le et al. 2023). In these scenarios, AGN feedback can either expel/heat or compress the gas in the interstellar medium (ISM), thus suppressing or enhancing star-forming activity in their hosts (e.g., Cresci et al. 2015a,b; Carniani et al. 2016; Bessiere & Ramos Almeida 2022). However, some studies do not reveal clear signatures of feedback. For instance, studies across various samples have identified flat relationships between the star-formation rate (SFR) and AGN luminosity (e.g.,

Harrison et al. 2012; Stanley et al. 2015; Schulze et al. 2019; Ramasawmy et al. 2019), suggesting a lack of clear evidence for the enhancement or suppression of star formation (Ruschel-Dutra et al. 2021). These findings underscore the complexity of AGN feedback and the intricate interactions between the nuclear activity and the ISM, challenging simplistic explanations.

AGN-driven gas outflows are one of the best tracers of AGN feedback. Over the past two decades, most previous works have focused on outflows traced by optical emission lines (e.g., Karouzos et al. 2016; Harrison et al. 2018). Studies on outflows involving different gas phases, such as warm molecular gas (e.g., rovibrational H $_2$ emission lines) in near-infrared (NIR) bands, are less common but gaining popularity (e.g., Storchi-Bergmann et al. 2009; U et al. 2013; Rupke & Veilleux 2013; Riffel et al. 2013, 2014; Izotov & Thuan 2016; Ramos Almeida et al. 2019; Riffel et al. 2020). Ionized gas and warm molecular gas are both important and complementary to each other, and comparative studies between them have garnered

significant interests in the field of AGN feeding and feedback, finding that different gas phases show different properties when tracing the feeding or feedback. For instance, in an Integral Field Spectroscopy (IFU) study, Storchi-Bergmann et al. (2009) suggested that H₂ gas traces the AGN feeding by the different intensity distribution compared with the bi-conic region detected by ionized gas. In contrast, also using IFU observations, Rupke & Veilleux (2013) revealed a compact disk and warm molecular outflow traced by H₂. The H₂ outflow gas has a bi-conic angle of 100 degrees and extends perpendicular to the disk up to a distance of 400 pc from the nucleus. Ramos Almeida et al. (2019) found that outflows of ionized gas are faster than those of warm molecular gas. In addition, they also found that warm molecular gas outflows have a significant impact on the host galaxy, suggesting that outflows traced by warm molecular H₂ gas may play an important role in regulating the growth of SMBHs and their host galaxies.

The general distinctions between the nature of warm molecular gas and ionized gas outflows remain unclear, including differences in size, kinematics, strength, and their impact on the surrounding ISM. These differences are crucial for comprehending the outflows and AGN feedback. Warm molecular gas, being cooler, is typically in the outer regions of the AGN structure. However, previous measurements of outflow sizes in the literature have predominantly relied on ionized gas, which is located in the inner parts of AGNs, potentially resulting in underestimation of the sizes of the outflows. Therefore, accurately estimating outflow sizes based on the kinematics of warm molecular gas is of significant importance. It is thus necessary to continue comparative studies between warm molecular gas and ionized gas with more samples.

While optical spectra of AGNs predominantly exhibit strong emission lines from ionized gas (e.g., Karouzos et al. 2016; Woo et al. 2016; Bae et al. 2017; Ruschel-Dutra et al. 2021), NIR spectra of AGNs offer the advantage of revealing emission lines from both ionized and warm molecular gas (e.g., Riffel et al. 2006, 2021a,b, 2023; Storchi-Bergmann et al. 2009; Rupke & Veilleux 2013; Ramos Almeida et al. 2019; Bianchin et al. 2022). Utilizing the Triple Spectrograph (TPSP; Herter et al. 2008), a NIR slit spectrograph, we can explore warm molecular gas outflows through ro-vibration H₂ emission lines, as well as ionized gas with multiple emission lines such as [S III] 0.9533 μ m, Pa α , and Pa β , among others. Our goal is to study the outflow kinematics for gas in different phases. By obtaining the radial profile of H₂ emission line, we will determine the kinematics of the warm molecular outflows and measure

the warm molecular outflow size. We will compare the sizes of outflows in different gas phases. In addition, we will also derive mass outflow rates and kinetic power of the warm molecular outflows and compare them with those of ionized gas outflows.

To facilitate a comprehensive comparison of outflow properties across different wavelength bands, it is essential for our sample to have undergone detailed optical observations. To achieve this, we follow the sample of 6 type-2 AGNs known for their extreme ionized outflows as studied by Karouzos et al. (2016). Karouzos et al. (2016) and Woo et al. (2016) carried out comprehensive examinations of outflows of ionized gas in these AGNs using IFU observations. These studies revealed a ring-like structure in the star-forming region at the edge of the outflow. Notably, these studies indicated an increase in SFRs following the increase of outflow strengths. However, a comprehensive exploration of warm molecular gas outflows in these specific objects is yet to be undertaken.

As the third paper of AGNSTRONG (Active Galactic Nuclei and STaR fOrmation in Nearby Galaxies; see [Paper-I](#), i.e., Le et al. 2024), we observed these 6 type-2 AGNs with TPSP and Double Spectrograph (DBSP) of the P200 telescope and obtained spectra in the UV-optical and NIR bands. Our analysis involves both integrated and spatially resolved measurements of strong emission lines from both ionized and warm molecular gas. We extract the outflowing components to measure the properties and compare the outflow size and kinematics between ionized and warm molecular gas. The paper is organized as follows: In Section 2, we outline the sample selection, details of target observations, and data reduction. Section 3 covers the extraction of integrated and spatially resolved spectra, as well as the fitting of emission lines using Gaussian models. Gas properties are estimated and the results are also presented in Section 3, which are discussed in Section 4. Finally, we summarize our work in Section 5. All spectra have been converted to the rest-frame wavelengths. Throughout this work, we adopt a flat Λ CDM cosmology with $\Omega_\Lambda = 0.7$, $\Omega_m = 0.3$, and $H_0 = 70 \text{ km s}^{-1} \text{ Mpc}^{-1}$.

2. SAMPLE AND DATA

2.1. Sample Selection

Karouzos et al. (2016) conducted a comprehensive analysis of six AGNs with prominent outflow signatures. They performed a detailed examination of the outflow kinematics of the [O III] and H α emission lines of these six AGNs using the Gemini Multi-Object Spectrograph (GMOS) IFU. However, a comprehensive investigation of warm molecular gas outflows in these specific objects

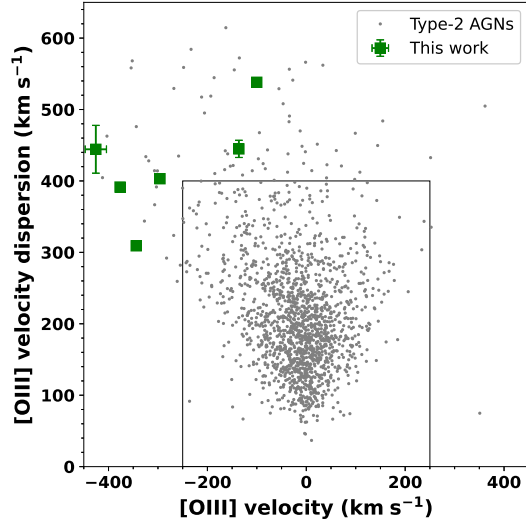


Figure 1. [O III] diagram of the luminosity-limited sample of AGNs with dust-corrected [O III] luminosity $L_{[O\ III];\text{cor}} > 10^{42}$ erg s $^{-1}$ and $z < 0.1$ from [Woo et al. \(2016\)](#). We highlight our sample of six type-2 AGNs using the green squares, while the solid box serves as a reference for high velocity ($|V| > 250$ km s $^{-1}$) or large velocity dispersion ($\sigma > 400$ km s $^{-1}$). Figure adapted from [Karouzos et al. \(2016\)](#).

has not yet been conducted. To delve deeper into the realm of warm molecular gas outflows and make comparisons between ionized and warm molecular gas properties, we conduct observations using the NIR and optical spectroscopy to detect both ionized and warm molecular gas in these six objects. These AGNs are type-2 Seyferts with $L_{[O\ III];\text{cor}} > 10^{42}$ erg s $^{-1}$ and serve as a complementary sample to [Paper-I](#), which focuses on type-1 AGNs, thereby providing a more comprehensive view. The target names are provided in Table 1, and a unique ID is assigned to each target, following an ascending order of right ascension.

The parent sample of these six AGNs was drawn from [Woo et al. \(2016\)](#). By selecting objects with sufficient signal-to-noise ratio (S/N) in both the continuum and emission lines, their sample comprised 38,948 type-2 AGNs. From this sample, [Karouzos et al. \(2016\)](#) selected 902 AGNs by limiting the redshift to $z < 1$ and requiring high luminosity, with extinction-corrected [O III] luminosity $L_{[O\ III];\text{cor}} > 10^{42}$ erg s $^{-1}$. Here, $L_{[O\ III];\text{cor}}$ refers to the [O III] luminosity corrected for extinction using the law of [Calzetti \(1999\)](#), following [Bae & Woo \(2014\)](#). Among these, 29 AGNs were further selected by [Karouzos et al. \(2016\)](#) for having high velocity ($|V| > 250$ km s $^{-1}$) or large velocity dispersion ($\sigma > 400$ km s $^{-1}$). The six AGNs are part of this subset and were observed with the

GMOS IFU ([Allington-Smith et al. 2002](#)) on Gemini-North ([Karouzos et al. 2016](#)). Their ionized gas exhibits robust outflow signatures, characterized by high velocities or large velocity dispersions, as illustrated in Figure 1 after redshift correction.

2.2. TPSP Observations

We conducted observations of these six type-2 AGNs using TPSP in the 2022A semester (ID: CTAP2022-A0037; PI: Huynh Anh N. Le). The wavelength coverage is 1.0–2.4 μm . The slit size is $1'' \times 30''$, with a scale of 0.28 arcsec per pixel along the slit. Figure 2 shows the slit overlaid on the SDSS images of the targets. The resolution of the instrument is approximately 50 km/s ($R = \lambda/\Delta\lambda = 2500$ –2700). Our observations were conducted in a nodding pattern ABBA, with the targets positioned differently along the slit in the A and B modes. A-B image differencing was performed to obtain the sky background spectrum for the other frame. The single exposure times for our target objects varied from 160 s to 500 s, as shown in Table 1. To correct telluric absorption lines in the NIR spectra of our sample, we observed several A0 V standard star spectra on the same night. The seeing conditions during our observations ranged from $2''$ to $2.5''$, while the airmass varied between 1.05 and 1.34. By analyzing the full width at half-maximum (FWHM) of five standard stars, we derived an approximate average seeing of $2.4''$ ([Rose et al. 2018](#); [Ramos Almeida et al. 2019](#)).

2.3. DBSP Observations

Three out of six sources in our sample were observed in the optical band by DBSP in the 2022 semester (ID: CTAP2022-A0024; PI: Luming Sun & Yibo Wang), providing the opportunity to study spatial properties with spatially resolved optical slit spectroscopy. DBSP is a grating spectrometer at the P200 Cassegrain focus, using a dichroic (D55 in this work) to split light into blue and red channels and observe simultaneously. The wavelength coverage is 3000–11000 Å. We used 600/4000 grating to detect high-resolution spectra, with the FWHM of the instrument being approximately 4.2 (6.0) Å for the blue (red) channel. The length of the slit is $128''$ and the width is $1.5''$. The spatial scale of the individual spatial pixels is $0.389''$ for the blue channel and $0.293''$ for the red channel. The exposure time is detailed in Table 1. The average seeing of DBSP observations is about $1.3''$.

2.4. Data Reduction

As described in [Paper-I](#), the data reduction for TPSP and DBSP observations is carried out using PypeIt

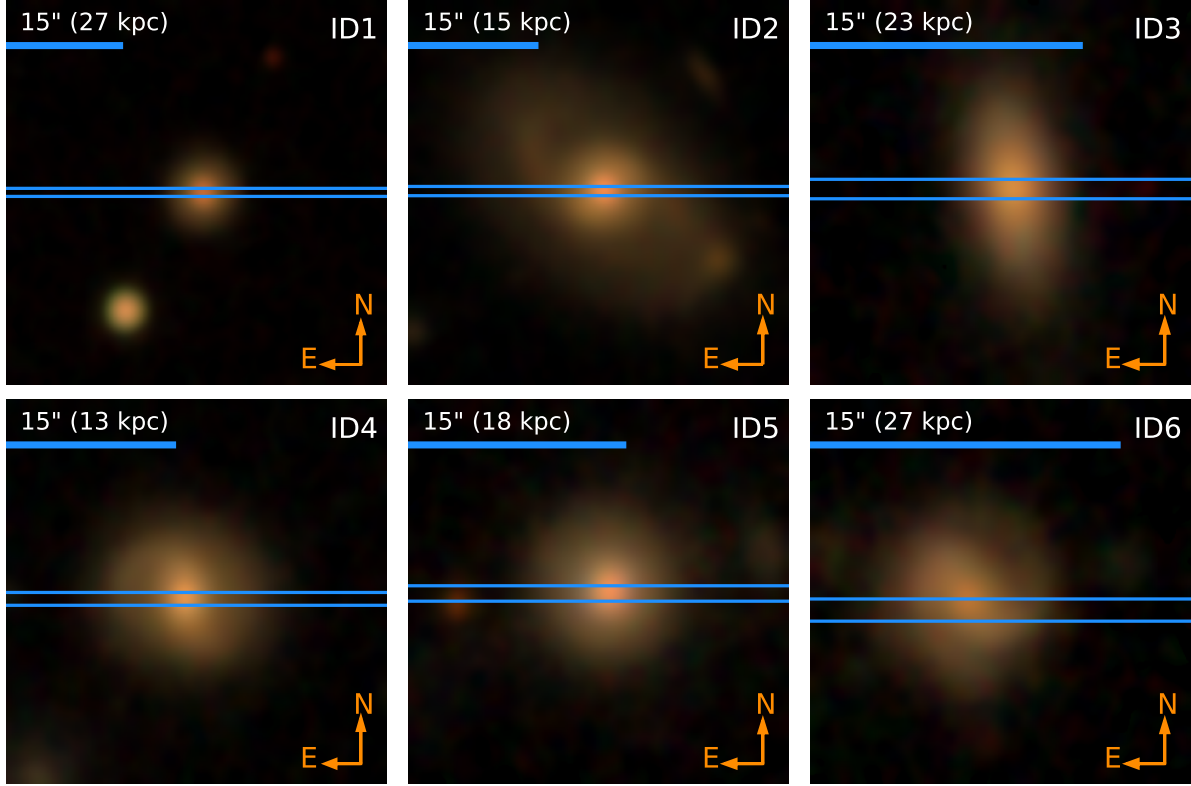


Figure 2. SDSS *gri* composite images of the targets. The blue solid lines show the direction of the slits of TPSP. The scale bar is displayed at the upper left corner of each panel, representing the scale of $15''$, and the corresponding spatial size is marked in brackets.

(Prochaska et al. 2020). It is a Python package for semi-automated reduction of spectroscopic data, supporting more than 20 spectrographs, including DBSP and TPSP. We follow the procedures outlined in the official cookbook for the flux calibration, co-adding of exposures, and telluric correction. The complete 1D NIR and optical spectra can be seen in Appendix A, shown in Figures A1 and A2, respectively. For the three AGNs without DBSP observations, we supplement the optical data with Sloan Digital Sky Survey (SDSS) spectra for our sample, which were analyzed by Karouzos et al. (2016).

To fully exploit the spatial resolution along the slit to investigate the spatial asymmetry of emission lines, we extract two-dimensional spectra. We apply offsets to the *trace* obtained from the 1D reduction process in the two-dimensional spectra to extract a series of 1D spectra. The *trace* represents the central position of the target on the slit. Subsequently, we follow the same procedures as the 1D reduction process for each extracted spectrum. Examples of 2D spectral images for TPSP and DBSP with the continuum removed are presented at the top of each image of Figures 3 and 4, respectively. The x-axis represents the rest-frame wavelength, while the y-axis corresponds to spatial pixels along the slit.

3. MEASUREMENTS AND RESULTS

3.1. Refining Redshifts

To better measure the emission line kinematics, we refine the redshifts estimated by Bae & Woo (2014) based on the optical spectra. This involves masking regions containing emission lines with broad components and conducting an initial spectral fit using Penalized Pixel-Fitting (pPXF, Cappellari 2022). pPXF is a versatile method adept at fitting a suite of templates, encompassing both stellar and gas components, to an observed spectrum. Given that all our targets are type-2 AGNs, we utilized E-MILES simple stellar population models (Vazdekis et al. 2016) and single Gaussian emission lines. pPXF provides estimates for stellar velocity (based on unrefined redshifts) and velocity dispersion based on the best-fit models. The stellar velocity is not negligible, reaching up to tens of km s^{-1} . The redshifts listed in Table 1 have been refined using the estimated stellar velocities, which differ by approximately 0.00005 compared to those measured by SDSS. The spectra utilized in this study have been adjusted according to these refined redshifts. Therefore, the [O III] velocity and velocity dispersion of the six selected AGNs (i.e., the green

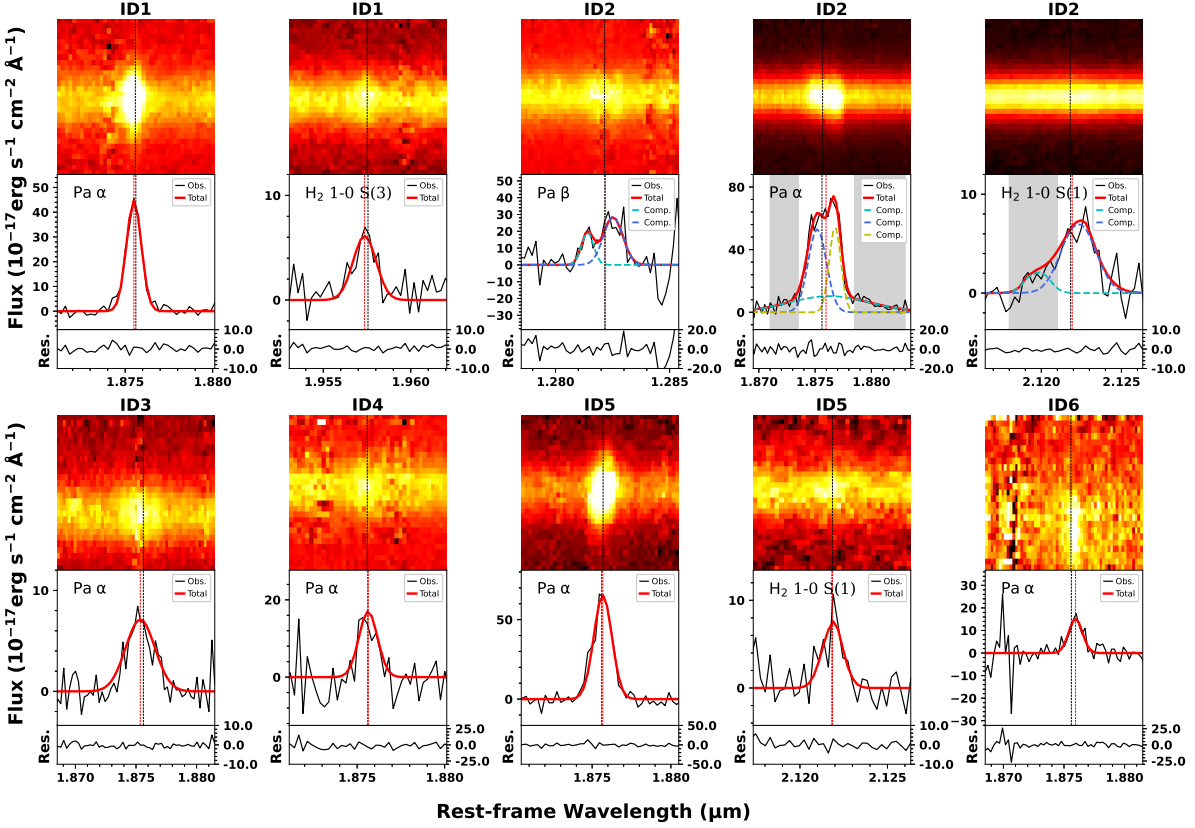


Figure 3. Examples of 2D spectral images and integrated emission line profiles for the TPSP observations. The images of 2D spectra close to the emission lines are shown in zscale following the IRAF zscale algorithm (top). The x-axis is the wavelength, and the y-axis is the spatial pixels on the slit. The observed integrated emission lines (black) are fitted with Gaussian profiles (middle). The red curve shows the best-fit model, while the blue, cyan, and yellow curves represent the individual Gaussian components in the double- and triple-Gaussian fits. The black dashed line represents the reference wavelength of each line, while the red dashed line represents the centroid wavelength of the total line profile. The residuals are shown at the bottom. The wavelength ranges used to estimate the outflow size are shaded.

squares in Figure 1) differ slightly from those in previous works (Karouzos et al. 2016; Woo et al. 2016).

3.2. Emission-line Fitting

We utilize Bayesian AGN Decomposition Analysis for SDSS Spectra (BADASS; Sexton et al. 2020) on the SDSS and DBSP spectra. BADASS fits various spectral components simultaneously, including the power-law continuum, stellar emission, and both the narrow and broad components of AGN emission lines. The fitting process is executed using Markov chain Monte Carlo techniques to provide robust uncertainties of the model parameters.

To remove the continuum contribution from the NIR spectra, we fit the spectral region adjacent to the emission line with a low-order polynomial while masking the emission line. The order of polynomials depends on the flatness of the spectra, typically requiring a first-degree polynomial in most instances. Subsequently, we utilize

`scipy.optimize.curve_fit` (Virtanen et al. 2020) to model the emission line profiles with one, two, or three Gaussian components as needed. As prior constraints, we specify the initial guesses as well as the lower and upper bounds for the Gaussian parameters (i.e., amplitude, central wavelength, and standard deviation) to ensure computational efficiency. In general, when a secondary component is indicated, we perform a double-Gaussian fit. However, if the S/N of the additional component is less than 3, we regard it as noise and discard it. In such cases, a single-Gaussian model is preferred. An analogous criterion is applied when a third component is introduced. We utilize the following formula to compute the S/N of the emission lines (or their components) (Le et al. 2015):

$$S/N = \frac{\sum_i (f_{L,i} - \bar{f}_C)}{\sigma(f_{C,i}) \sqrt{n_L(1 + 1/n_C)}}, \quad (1)$$

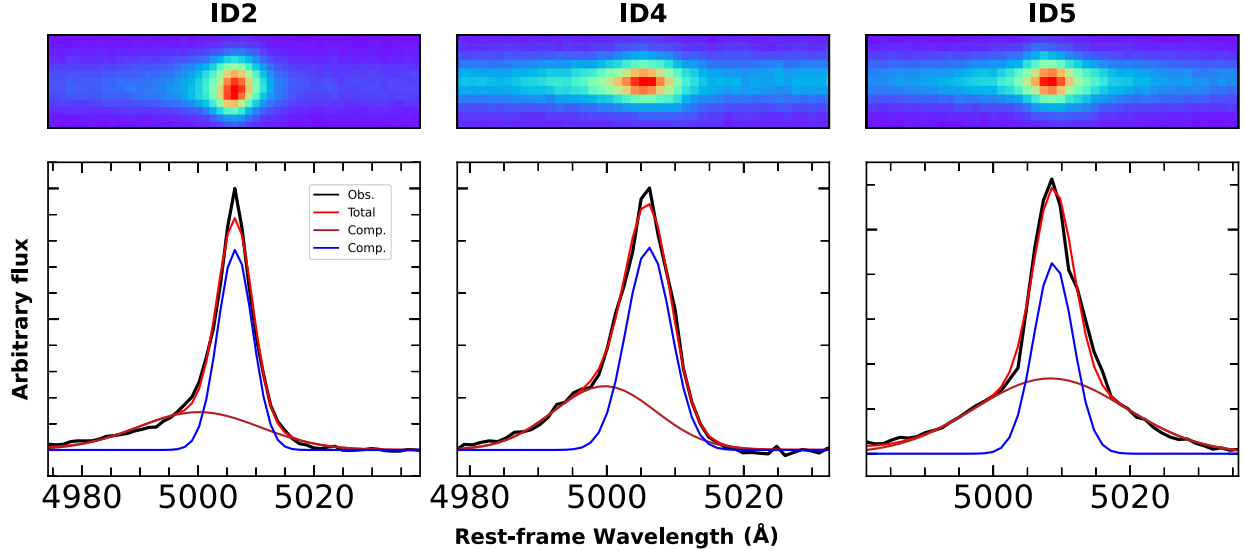


Figure 4. Examples of 2D spectral images and integrated emission line profiles of optical [O III] emission lines in the DBSP observations. On the top are the images of 2D spectra. The observed integrated emission lines (black) are fitted with Gaussian profiles. The red curve shows the best-fit model, while the blue and brown curves represent the individual Gaussian components.

Table 1. Observational Log

ID	SDSS Name	Redshift	m_K (mag)	$\log L_{[O\ III]};\text{cor}$ (erg s $^{-1}$)	Instrument	Observational Date	Exposure Time (s)
(1)	(2)	(3)	(4)	(5)	(6)	(7)	(8)
1	J091807.52+343946.0	0.0973	13.5	42.9	TPSP	2022 Feb 10	500×4
2	J113549.08+565708.2	0.0514	11.4	43.1	TPSP/DBSP	2022 Feb 10/2022 Apr 21	240×4/500
3	J140452.65+532332.1	0.0813	13.5	42.6	TPSP	2022 Feb 10	250×8
4	J160652.16+275539.0	0.0461	12.7	42.2	TPSP/DBSP	2022 Feb 10/2022 Jun 29	160×4/600
5	J162232.68+395650.2	0.0631	13.4	42.4	TPSP/DBSP	2022 Feb 10/2022 Jun 29	240×4/600
6	J172037.94+294112.4	0.0995	14.4	42.3	TPSP	2022 Feb 10	200×8

NOTE—Columns are as follows: (1) ID of our objects; (2) Name of the counterpart in SDSS; (3) Redshift refined using the estimated stellar velocities; (4) K-band magnitude; (5) Dust-corrected [O III] luminosity (Karouzos et al. 2016); (6) Instrument for observation; (7) Observational date; (8) Total exposure time.

where $\sum_i(f_{L,i} - \bar{f}_C)$ is the intensity of the line (or their components) after continuum subtraction and $\sigma(f_{C,i})$ denotes the standard deviation of the continuum. $\sqrt{n_L(1 + 1/n_C)}$ serves as a statistical correction term, where n_L and n_C represent the numbers of data points for the line and continuum, respectively. Illustrative examples of the integrated emission-line fittings and their residuals are displayed at the bottom of each panel of Figures 3 and 4.

Further analyses are based on the Gaussian profiles of the emission lines (see Paper-I). The velocity and velocity dispersion of the gas are measured using the 1st (λ_0)

and 2nd moments (σ) of the profile:

$$\lambda_0 = \frac{\sum \lambda f_\lambda}{\sum f_\lambda}, \quad (2)$$

and

$$\sigma_\lambda^2 = \frac{\sum (\lambda - \lambda_0)^2 f_\lambda}{\sum f_\lambda}. \quad (3)$$

And the velocity and velocity dispersion can be written as

$$V = c \frac{\lambda_0 - \lambda_{\text{rest}}}{\lambda_{\text{rest}}}, \quad (4)$$

and

$$\sigma = c \frac{\sigma_\lambda}{\lambda_{\text{rest}}}, \quad (5)$$

Table 2. NIR Emission line properties and components.

ID	Line	Comp.	Flux (10^{-17} erg s $^{-1}$ cm $^{-2}$)	V (km s $^{-1}$)	σ (km s $^{-1}$)	FWHM (km s $^{-1}$)	R_{NLR} (kpc)	S/N
(1)	(2)	(3)	(4)	(5)	(6)	(7)	(8)	(9)
1	He I 1.0832	T	132.1 $^{+2.9}_{-3.0}$	4.5 $^{+2.6}_{-3.0}$	98.5 $^{+3.3}_{-3.3}$	232.1 $^{+7.9}_{-7.8}$...	6.4
	Pa α 1.8756	T	476.6 $^{+7.0}_{-6.5}$	-17.9 $^{+1.1}_{-1.1}$	47.5 $^{+1.6}_{-1.8}$	111.8 $^{+3.8}_{-4.3}$	0.38 $^{+0.01}_{-0.01}$	34.3
	H ₂ 1-0 S(3) 1.9576	T	101.4 $^{+7.0}_{-7.3}$	-29.7 $^{+8.0}_{-7.9}$	87.6 $^{+12.2}_{-11.3}$	206.3 $^{+28.8}_{-26.7}$	0.60 $^{+0.07}_{-0.07}$	9.2
2	[S III] 0.9533	T	2048.4 $^{+17.3}_{-18.3}$	69.4 $^{+2.1}_{-2.2}$	196.2 $^{+2.4}_{-2.2}$	462.1 $^{+5.8}_{-5.2}$	0.25 $^{+0.01}_{-0.01}$	27.8
	He I 1.0832	T	1658.9 $^{+12.7}_{-12.6}$	-34.2 $^{+2.7}_{-3.0}$	279.9 $^{+3.6}_{-3.6}$	487.5 $^{+8.5}_{-8.5}$...	28.4
	1		1321.1 $^{+26.9}_{-37.0}$	-55.7 $^{+5.2}_{-5.9}$	305.0 $^{+5.8}_{-5.3}$	718.4 $^{+13.6}_{-12.4}$...	22.1
	2		338.2 $^{+40.5}_{-28.2}$	49.2 $^{+3.2}_{-3.8}$	104.5 $^{+8.5}_{-6.4}$	246.1 $^{+19.9}_{-15.1}$...	9.3
	[Fe II] 1.2570	T	241.2 $^{+6.9}_{-6.7}$	9.7 $^{+5.0}_{-4.6}$	165.1 $^{+3.1}_{-2.5}$	472.7 $^{+9.8}_{-12.3}$...	8.9
	1		143.7 $^{+13.1}_{-13.2}$	-103.1 $^{+19.7}_{-17.7}$	108.4 $^{+14.6}_{-14.8}$	255.2 $^{+34.4}_{-34.8}$...	5.9
	2		97.5 $^{+14.3}_{-13.8}$	177.3 $^{+11.3}_{-13.3}$	53.2 $^{+11.9}_{-10.5}$	125.3 $^{+28.0}_{-24.6}$...	5.1
	Pa β 1.2822	T	439.0 $^{+97.1}_{-14.4}$	8.0 $^{+3.4}_{-3.1}$	141.4 $^{+2.8}_{-2.5}$	409.6 $^{+7.3}_{-409.6}$	0.06 $^{+0.04}_{-0.04}$	11.0
	1		128.7 $^{+296.2}_{-7.9}$	-176.8 $^{+142.0}_{-4.0}$	36.5 $^{+95.9}_{-5.4}$	86.1 $^{+226.0}_{-12.8}$...	4.7
	2		302.7 $^{+16.5}_{-184.1}$	85.8 $^{+90.8}_{-6.9}$	85.0 $^{+4.7}_{-85.0}$	200.1 $^{+11.0}_{-200.1}$...	8.9
3	[Fe II] 1.6440	T	244.8 $^{+8.2}_{-7.9}$	21.6 $^{+7.8}_{-7.6}$	193.4 $^{+6.1}_{-5.8}$	455.4 $^{+14.4}_{-13.6}$...	10.4
	Pa α 1.8756	T	2720.3 $^{+35.6}_{-31.0}$	57.8 $^{+7.0}_{-8.1}$	359.1 $^{+19.8}_{-16.7}$	486.8 $^{+3.3}_{-4.9}$	0.17 $^{+0.00}_{-0.00}$	41.2
	1*		927.2 $^{+35.1}_{-39.2}$	105.7 $^{+23.7}_{-25.5}$	570.3 $^{+38.0}_{-30.4}$	1343.0 $^{+89.5}_{-71.7}$...	11.1
	2		1083.5 $^{+56.0}_{-57.3}$	-66.9 $^{+7.5}_{-8.2}$	120.3 $^{+6.0}_{-5.9}$	283.3 $^{+14.1}_{-14.0}$...	26.9
	3		711.9 $^{+52.0}_{-50.4}$	185.4 $^{+4.2}_{-4.5}$	66.9 $^{+3.9}_{-3.8}$	157.6 $^{+9.3}_{-9.0}$...	22.9
	H ₂ 1-0 S(1) 2.1218	T	245.8 $^{+19.2}_{-17.2}$	11.6 $^{+19.5}_{-19.6}$	197.5 $^{+22.3}_{-16.0}$	350.2 $^{+139.6}_{-89.2}$	0.25 $^{+0.01}_{-0.01}$	13.9
	1*		44.0 $^{+152.3}_{-20.8}$	-288.6 $^{+277.9}_{-79.0}$	81.6 $^{+127.0}_{-81.6}$	192.1 $^{+299.1}_{-192.1}$...	3.1
	2		197.5 $^{+30.3}_{-146.8}$	73.3 $^{+57.2}_{-21.5}$	135.4 $^{+38.7}_{-108.1}$	318.8 $^{+91.1}_{-254.5}$...	12.3
	Br γ 2.1661	T	193.8 $^{+20.3}_{-20.0}$	14.8 $^{+19.9}_{-21.8}$	168.3 $^{+22.1}_{-20.5}$	396.4 $^{+52.1}_{-48.4}$	0.19 $^{+0.08}_{-0.08}$	9.3
	[S III] 0.9533	T	429.8 $^{+11.3}_{-10.4}$	-150.2 $^{+8.5}_{-7.6}$	263.1 $^{+7.5}_{-7.8}$	619.7 $^{+17.6}_{-18.3}$...	10.1
4	He I 1.0832	T	180.7 $^{+4.3}_{-4.5}$	1.4 $^{+6.8}_{-6.0}$	215.4 $^{+5.4}_{-5.0}$	507.2 $^{+12.7}_{-11.9}$...	6.8
	Pa α 1.8756	T	216.2 $^{+6.5}_{-6.1}$	-41.1 $^{+5.9}_{-5.9}$	187.8 $^{+7.2}_{-6.2}$	442.3 $^{+17.0}_{-14.7}$	0.55 $^{+0.07}_{-0.07}$	16.3
	He I 1.8702	T	214.4 $^{+41.4}_{-53.4}$	17.6 $^{+28.1}_{-13.2}$	31.9 $^{+10.3}_{-31.9}$	75.2 $^{+24.4}_{-75.2}$...	3.7
5	Pa α 1.8756	T	228.7 $^{+20.6}_{-19.9}$	3.2 $^{+9.0}_{-8.6}$	69.9 $^{+10.8}_{-10.6}$	164.7 $^{+25.4}_{-24.9}$...	7.2
	[S III] 0.9533	T	1271.6 $^{+20.6}_{-20.8}$	5.6 $^{+2.4}_{-2.4}$	108.1 $^{+2.1}_{-2.1}$	254.5 $^{+4.9}_{-4.8}$	0.18 $^{+0.29}_{-0.29}$	12.0
	He I 1.0832	T	848.9 $^{+14.3}_{-15.4}$	64.4 $^{+3.5}_{-3.7}$	186.5 $^{+4.5}_{-4.9}$	439.2 $^{+10.6}_{-11.7}$	0.15 $^{+0.14}_{-0.14}$	10.3
	Pa γ 1.0941	T	154.3 $^{+8.4}_{-7.6}$	9.1 $^{+6.0}_{-5.9}$	66.7 $^{+3.8}_{-4.2}$	157.0 $^{+8.9}_{-10.0}$...	4.0
	He II 1.2304	T	307.3 $^{+27.0}_{-28.5}$	97.2 $^{+3.7}_{-4.2}$	8.8 $^{+7.6}_{-8.8}$	20.8 $^{+18.0}_{-20.8}$...	9.9
	[Fe II] 1.2570	T	289.6 $^{+8.0}_{-7.8}$	-21.3 $^{+3.2}_{-3.2}$	136.5 $^{+8.5}_{-7.7}$	321.5 $^{+19.9}_{-18.1}$	0.66 $^{+0.12}_{-0.12}$	8.7
	[Fe II] 1.6440	T	214.8 $^{+3.8}_{-3.8}$	-23.9 $^{+2.3}_{-2.3}$	97.6 $^{+1.9}_{-2.1}$	229.8 $^{+4.6}_{-4.9}$...	9.7
	Pa α 1.8756	T	939.0 $^{+9.3}_{-8.3}$	10.8 $^{+1.0}_{-1.0}$	77.5 $^{+1.2}_{-1.4}$	182.6 $^{+2.8}_{-3.3}$	0.13 $^{+0.04}_{-0.04}$	27.7
	H ₂ 1-0 S(1) 2.1218	T	110.8 $^{+21.3}_{-20.4}$	6.0 $^{+19.0}_{-19.0}$	66.6 $^{+24.4}_{-34.7}$	156.9 $^{+57.4}_{-81.7}$...	6.4
	Pa α 1.8756	T	214.6 $^{+14.0}_{-11.6}$	54.9 $^{+6.0}_{-6.5}$	76.3 $^{+8.4}_{-9.0}$	179.8 $^{+19.7}_{-21.1}$...	5.1

NOTE—Columns are as follows: (1) ID of our objects; (2) the name and wavelength in μm of the line; (3) the components of the model, with T indicating the total profile and 1, 2, and 3 denoting the individual components; (4) the flux of the model profile; (5) the centroid velocity of the profile; (6) the velocity dispersion of the profile; (7) the FWHM of the profile; (8) the radius of the NLR size estimated from the total profile, and the dots imply that the lines or components are not spatially resolved; (9) the signal-to-noise ratio of the continuum-free emission lines. Bold numbers denote components with high velocities ($|V| > 250$ km s $^{-1}$) or large velocity dispersions ($\sigma > 400$ km s $^{-1}$), which are thought to be signatures of significant outflows. The corresponding component numbers are marked with an asterisk.

where c is the speed of light and λ_{rest} is the rest-frame wavelength of the emission lines, derived using the redshift corrected for the systemic velocity as described in Section 3.1. The [O III] velocity and velocity dispersion in our sources are shown as green squares in Figure 1. The results of the NIR spectral fitting are summarized in Table 2. We detect $\text{Pa}\alpha$ 1.8756 μm in all 6 targets, He I 1.0832 μm in 4 targets, and [S III] 0.9533 μm in 3 targets. The [Fe II] 1.2570 μm , [Fe II] 1.6440 μm , H_2 1-0 S(3) and H_2 1-0 S(1) are detected in 2 targets each. However, in ID 2, H_2 1-0 S(3) is blended with [S VI] 1.9630, and the parameters for these two lines are not listed in Table 2. The remaining lines ($\text{Pa}\beta$ 1.2822 μm , $\text{Pa}\gamma$ 1.0941 μm , $\text{Br}\gamma$ 2.1661 μm , He II 1.2304 μm , and He I 1.8702 μm) are each detected in only one source. For ID 1, 3, 4, 5, and 6, all emission lines are adequately fitted with a single-Gaussian model. In ID 2, four lines (He I 1.0832 μm , [Fe II] 1.2570 μm , $\text{Pa}\beta$, H_2 1-0 S(1)) require a double-Gaussian model, while one line ($\text{Pa}\alpha$) is fitted with a triple-Gaussian model. In all cases where a multi-Gaussian fitting is adopted, the individual components are reported explicitly in Table 2. Bold numbers denote components with high velocities ($|V| > 250 \text{ km s}^{-1}$) or large velocity dispersions ($\sigma > 400 \text{ km s}^{-1}$), which are adopted as reference criteria for identifying components associated with significant outflows. Therefore, signatures of outflows (both ionized and molecular) are found only in ID 2 in the NIR observations. However, as discussed by Zhang et al. (2011); Le et al. (2023), decomposing emission-line profiles into multiple Gaussian components can be artificial. Therefore, the identification of significant outflow components should be regarded as indicative only and interpreted with caution.

The bootstrap method, noted for its versatility (Rice 2007), serves as our approach to estimating uncertainties. The spectral errors estimated by PypeIt are assumed to follow a normal distribution with a standard deviation corresponding to the errors at each wavelength. Subsequently, we resample the spectra based on the distributions, conducting 1000 iterations of fitting the new spectra. We calculate the 16th and 84th percentiles of the obtained parameters to estimate their 1σ uncertainties, with the median serving as the reliable result. Note that the sum of the medians is not strictly equal to the median of the sum. This explains the slight deviation between the summed components and the total measurements in Table 2.

3.3. Spatially Resolved Kinematics

TPSP provides us with spatially-resolved measurements over several kilo-parsec scales along the slit di-

rection, enabling us to examine the kinematics of both the ionized and warm molecular gas. Empirically, spectra extracted from a single pixel may not have sufficient strength to discern the line profile due to noise for TPSP observations. Therefore, we employ a 3-pixel binning method (0.28''/pixel, about 1/3 of the average seeing) and measure the binned line profiles as described in Section 3.2. Note that, as an empirical choice, using the binning size of about 1/3 of the seeing, whether in images or spectra, is generally considered to help avoid oversampling without significantly sacrificing resolution (Kaastra & Bleeker 2016).

We investigate how the kinematics of the ionized and warm molecular gas vary as a function of distance from the nucleus to the outer regions of the AGN. For this purpose, we use the $\text{Pa}\alpha$ and H_2 1-0 S(1) lines to represent the ionized and warm molecular gas, respectively, as shown in Figure 5. Note that though we observed H_2 1-0 S(1) line in ID 5, we found it did not exhibit sufficient spatial resolution. Among our sample, only source ID 2 shows clear outflow signatures in the NIR band. This source also displays enhanced velocity dispersion and an irregular spatial distribution. The gas kinematics in this source is therefore primarily dominated by outflows.

For sources with DBSP observations, the kinematics of [O III] is shown in lighter colors for comparison in both Figures 5 and 6.

Similar to the analysis of kinematics distribution, we present the velocity and velocity dispersion of the emission lines as a function of aperture diameter (see Figure 6). We examine the kinematic disparity between the inner and outer regions of each galaxy using a range of aperture sizes, spanning from $\sim 1''$ to $\sim 5''$. We see no significant trends in the velocity dispersion toward the outer regions. Note that in both Figures 5 and 6, the velocity and velocity dispersion correspond to the total line profile, since the spatially resolved spectra cannot be consistently and reliably fitted with multi-Gaussian models. Nevertheless, it is clear that the velocity dispersion of source ID 2 is significantly higher than that of the other sources, with the peak σ exceeding that of the others by more than 100 km s^{-1} .

3.4. Narrow-line Region Size

We present examples of NIR 2D spectra in Figure 3, most of which exhibit features of spatial extension. Asymmetry also appears in some images, e.g., $\text{Pa}\alpha$ of ID 2. The blue-shifted component exhibits a displacement towards the north in the image, whereas the red-shifted component displays a displacement towards the south.

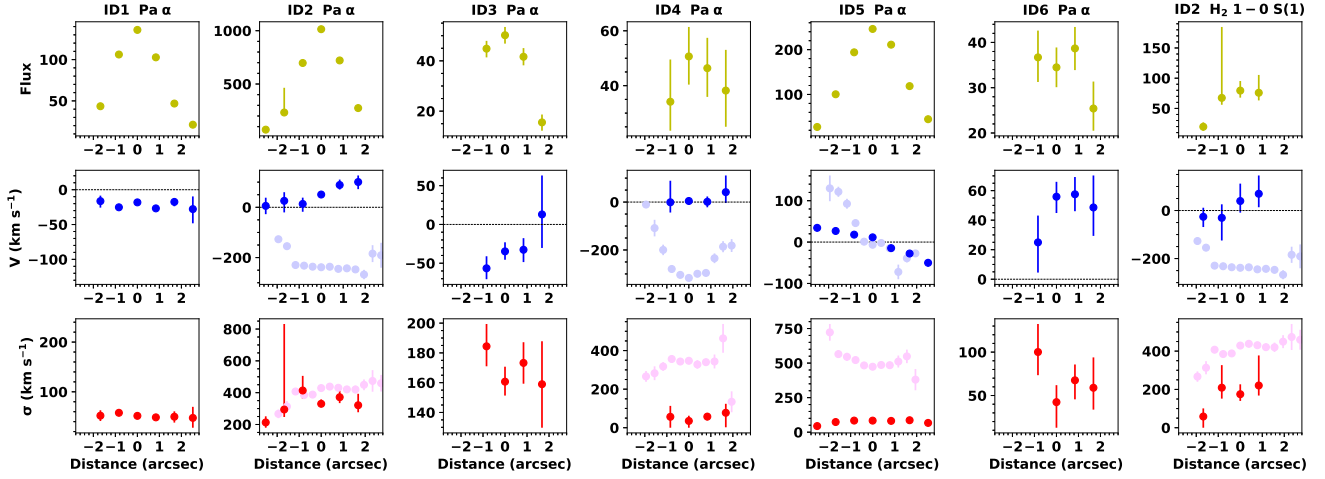


Figure 5. Distributions of flux (yellow dots), velocity (blue), and velocity dispersion (red) of emission lines along the slits. The NIR data are binned with a size of 3 pixels, and the kinematics of optical [O III] lines is shown in light blue and magenta without binning.

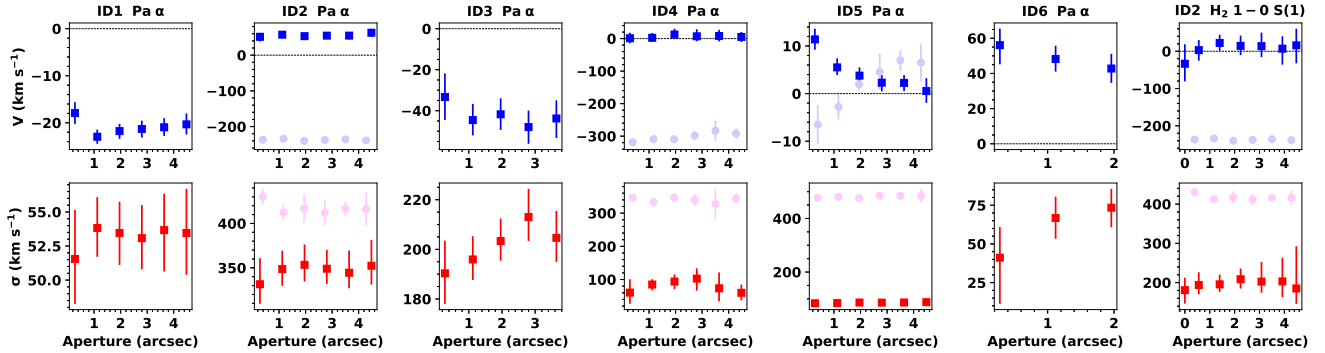


Figure 6. Velocity (blue) and velocity dispersion (red) of NIR emission lines as a function of aperture diameter. The kinematics of optical [O III] lines is shown in light blue and magenta.

To fully exploit the spatial resolution potential of TPSP, we investigate the radius of the narrow-line region (NLR) size with emission lines that are sufficiently strong. We sum up the flux in the region close to the emission lines with the continuum removed for each spatial slice along the slit and fit the spatial profiles with a single Gaussian. Given the varying seeing conditions and redshifts of our target sources, not all of our sources are spatially resolved. Following the criteria outlined by Rose et al. (2018) and Ramos Almeida et al. (2019), we consider targets to be spatially resolved when the FWHM measurements taken from emission lines are more than 3σ larger than the FWHM measured in the same region from the standard stars. The radius of NLR (R_{NLR}) on the slit can be calculated as

$$R_{\text{NLR}} = \frac{1}{2} \sqrt{\text{FWHM}_{\text{obs}}^2 - \text{FWHM}_{\text{seeing}}^2}, \quad (6)$$

where the $\text{FWHM}_{\text{seeing}}$ is carefully measured using the same method as FWHM_{obs} , with the spectra of stan-

dard stars in the wavelength range close to the emission line. When the size of NLR notably surpasses the seeing (Rose et al. 2018), it is considered to be resolved:

$$\text{FWHM}_{\text{obs}} \geq \text{FWHM}_{\text{seeing}} + 3\sigma, \quad (7)$$

where σ is the uncertainty of the seeing. The results are shown in column (8) of Table 2. Note that the spatial profiles may be partially obscured by noise, which could lead to an underestimation of the sizes.

3.5. Mass of Ionized and Warm Molecular Gas

Utilizing the fluxes of H_2 1-0 S(1), $\text{Pa}\alpha$, $\text{Br}\gamma$, and $\text{Pa}\beta$ emission lines, it is possible to derive the masses of the warm molecular gas and the ionized gas. Specifically, the mass of the warm molecular gas can be estimated by (Scoville et al. 1982; Riffel et al. 2014, 2023; Bianchin et al. 2022)

$$\left(\frac{M_{\text{H}_2}}{M_{\odot}}\right) = 5.0776 \times 10^{13} \left(\frac{F_{\text{H}_2 \text{ 1-0 S(1)}}}{\text{erg s}^{-1} \text{ cm}^{-2}}\right) \left(\frac{D}{\text{Mpc}}\right)^2, \quad (8)$$

where $F_{\text{H}_2 \text{ 1-0 S(1)}}$ represents the flux of the H_2 1-0 S(1) emission line, and D denotes the luminosity distance calculated using the redshift of the galaxy, assuming thermodynamic equilibrium with an excitation temperature of 2000 K. In our sample, two H_2 1-0 S(1) lines are detected. And consequently, the mass of warm molecular gas for ID 2 is estimated to be $\log(M_{\text{gas}}/M_{\odot}) = 3.82^{+0.03}_{-0.03}$, while for ID 5, it is $\log(M_{\text{gas}}/M_{\odot}) = 3.65^{+0.08}_{-0.09}$.

The mass of the ionized gas can be estimated using (Rose et al. 2018):

$$M = \frac{L(\text{H}\beta)m_p}{\alpha_{\text{H}\beta}^{\text{eff}}h\nu_{\text{H}\beta}n_e}, \quad (9)$$

where m_p is the proton mass, h is the Planck constant, $\nu_{\text{H}\beta}$ is the rest-frame frequency of the $\text{H}\beta$ transition, and n_e is the electron density of the gas. $\alpha_{\text{H}\beta}^{\text{eff}}$ denotes the effective Case B recombination coefficient for $\text{H}\beta$ assuming electron temperature $T_e \approx 10^4$ K (consistent with the temperature estimated for IDs 2 and 5). Finally, $L(\text{H}\beta)$ denotes the $\text{H}\beta$ luminosity, which is inferred from the detected emission lines using the theoretical Case B ratios, e.g., $F(\text{Pa}\alpha)/F(\text{H}\beta) \approx 0.332$, $F(\text{Pa}\beta)/F(\text{H}\beta) \approx 0.163$, and $F(\text{Br}\gamma)/F(\text{H}\beta) \approx 0.028$ (Storey & Hummer 1995; Osterbrock & Ferland 2006). The distances are calculated from the redshifts listed in Table 1. Since $\text{Pa}\alpha$ is detected in all targets and the electron densities n_e are derived from the [S II] doublet for each source (see Appendix A), we estimate the ionized gas masses to be $\log(M_{\text{gas}}/M_{\odot}) = 6.28^{+0.01}_{-0.01}$, $6.90^{+0.01}_{-0.01}$, $7.39^{+0.01}_{-0.01}$, $6.45^{+0.04}_{-0.04}$, $6.89^{+0.00}_{-0.00}$, and $7.42^{+0.03}_{-0.02}$ for IDs 1–6, respectively.

Similarly, since the $\text{Pa}\beta$ and $\text{Br}\gamma$ lines are detected in ID 2, we additionally estimate the ionized gas mass from these lines to be $\log(M_{\text{gas}}/M_{\odot}) = 6.43^{+0.09}_{-0.01}$ and $6.85^{+0.04}_{-0.05}$, respectively. The estimate based on $\text{Br}\gamma$ is consistent with that derived from $\text{Pa}\alpha$, whereas the estimate based on $\text{Pa}\beta$ is lower. This deviation may be caused by telluric absorption, as the $\text{Pa}\beta$ line lies close to a wavelength range that is strongly affected by sky emission (see Figure A1). Therefore, we adopt the ionized gas mass derived from $\text{Pa}\alpha$ as our fiducial estimate for ID 2.

3.6. Outflow Properties

We determine the wavelength ranges used to estimate the outflow size following the same procedure described in Section 3.4. The wavelength ranges are shaded in Figure 3 for lines with significant outflow components, as marked with an asterisk in Table 2. The spatial profiles of the continuum-subtracted outflow components for these lines ($\text{Pa}\alpha$, and H_2 1-0 S(1)) are shown in Figure 7. We see that the profile of H_2 is skewed to the left,

indicating that the intensity distribution of the warm molecular outflow is different from that of the ionized outflow in ID 2. Similar to Equation (6), the outflow size is calculated by

$$R_{\text{out}} = \frac{1}{2} \sqrt{\text{FWHM}_{\text{obs}}^2 - \text{FWHM}_{\text{seeing}}^2}. \quad (10)$$

The outflow sizes estimated from these two lines are $0.66^{+0.02}_{-0.02}$ kpc and $0.87^{+0.20}_{-0.20}$ kpc, respectively. Compared to the outflow size estimated from the ionized emission lines, the size inferred from the warm molecular lines is larger, albeit with a broad range of uncertainties.

Assuming that the outflow is traced with component with high velocities or large velocity dispersions, we use the fluxes of the outflow H_2 1-0 S(1) and $\text{Pa}\alpha$ components to calculate the outflow masses via Equation (9), adopting the same electron densities as those used for the NLR (see Appendix A).

Assuming a biconical outflow model (Bae & Woo 2016), we estimate the maximum outflow velocity by adding velocity dispersion σ to the systemic velocity V (Ayubinia et al. 2023):

$$V' = 2\sqrt{V^2 + \sigma^2}. \quad (11)$$

The outflow rates of mass and energy are calculated as (González-Alfonso et al. 2017; Ayubinia et al. 2023)

$$\dot{M}_{\text{out}} = 3\left(\frac{M_{\text{out}}V'}{R_{\text{out}}}\right), \text{ and} \quad (12)$$

$$\dot{E}_{\text{out}} = \frac{1}{2}\dot{M}_{\text{out}}V'^2. \quad (13)$$

We list the results of the outflow properties in Table 3. Note that these results largely depend on the assumptions and the procedure of measurements (Hervella Seoane et al. 2023). The potential outflow components may also be largely submerged in the noise for most of the NIR emission lines in this work.

4. DISCUSSIONS

4.1. AGN Strength and Kinematics

Despite large scatters, outflows with the highest velocities were found to be driven by the most luminous AGNs (e.g., Fiore et al. 2017; Ayubinia et al. 2023). This correlation can be seen in the NIR ionized lines in our sample (as shown in Figure 8), whereas the data for the warm molecular line is too limited to discern a trend. The Spearman correlation coefficient, estimated using `scipy.stats.spearmanr`, is 0.63 (0.54) with an associated p -value of 0.02 (0.04) for the ionized lines (both the ionized and warm molecular lines). Note that V' here indicates the outflow velocity only if the outflow

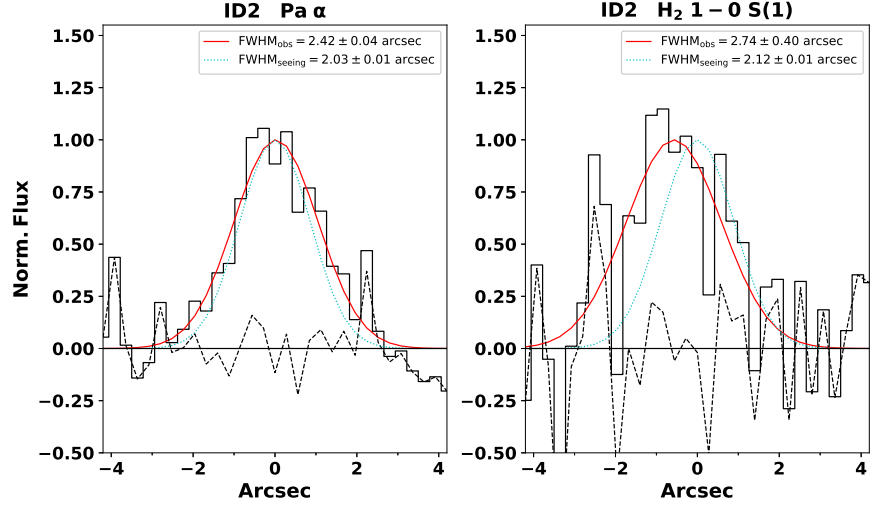


Figure 7. Spatial profiles of the continuum-subtracted outflow components for $\text{Pa}\alpha$ and H_2 1-0 S(1). The fluxes have been normalized by the peak values of the fitted Gaussian profiles, which are represented by the red lines. The residuals are indicated by the dotted lines and the cyan dotted lines correspond to the seeing FWHM.

Table 3. Properties of the ionized and warm molecular gas and outflows in ID 2.

ID	phase	$\log M_{\text{gas}}$ (M_{\odot})	f	R_{out} (kpc)	V' (km/s)	$\log M_{\text{out}}$ (M_{\odot})	$\log \dot{M}_{\text{out}}$ ($M_{\odot} \text{ yr}^{-1}$)	$\log \dot{E}_{\text{out}}$ (erg s^{-1})
(1)	(2)	(3)	(4)	(5)	(6)	(7)	(8)	(9)
2	ionized	$6.90^{+0.01}_{-0.00}$	0.34	$0.66^{+0.02}_{-0.02}$	$727.48^{+38.73}_{-33.14}$	$6.43^{+0.02}_{-0.02}$	$0.96^{+0.03}_{-0.03}$	$42.18^{+0.07}_{-0.07}$
2	warm molecular	$3.82^{+0.03}_{-0.03}$	0.20	$0.87^{+0.20}_{-0.20}$	$399.08^{+45.22}_{-32.50}$	$3.11^{+0.62}_{-0.29}$	$-2.68^{+0.56}_{-0.37}$	$38.05^{+0.55}_{-0.42}$

NOTE—(1) Sample ID; (2) the gas phase, either warm molecular or ionized gas; (3) the mass of warm molecular or ionized gas estimated by the flux of the line; (4) the outflow fraction $f = \frac{M_{\text{out}}}{M_{\text{gas}}}$; (5) the mean value of the radius of the bulk of outflow; (6) the mean value of the velocity of the bulk of outflow; (7) the total mass of the bulk of outflow; (8) the mass outflow rate of the outflow; (9) the outflow power.

exists. If no outflow is present, it merely serves as a parameter to describe the kinematics of the gas. We confirm that if we use only the velocity dispersion σ of these lines, which dominates the value of V' , the positive correlation persists, with a correlation coefficient of 0.68 (0.57) and a p -value of 0.01 (0.03) for the ionized lines (both the ionized and warm molecular lines). However, our selected sample is small and has a narrow range of luminosity. The analysis of a larger sample is necessary to confirm this relation.

4.2. AGN Strength and Narrow-line Region Size

Size-luminosity relation has been found in NLR size R_{NLR} and [O III] luminosity $L_{[\text{O III}]}$ (Le et al. 2017a). We present the NLR sizes of our sample estimated based on spatially resolved emission lines, including both ionized and warm molecular gases in Figure 9.

The archival samples are collected from Husemann et al. (2013), Husemann et al. (2014), Karouzos et al. (2016), Bae et al. (2017), and Le et al. (2017a). For coherence with the comparisons, we take the bolometric luminosity (calculated from extinction-uncorrected [O III] luminosity, $L_{\text{bol}} = 3500 \times L_{[\text{O III}]}$; Heckman et al. 2004) as an indicator of AGN strength.

We find that ionized lines exhibit similar characteristics in this diagram, whether observed in the infrared or optical. We note that only two H_2 1-0 S(1) lines have been detected, and thus we cannot draw a conclusive trend for warm molecular lines. We cannot see a clear distinction between [O III] and other lines, as we expect [S III], He I, H_2 and $\text{Pa}\alpha$ to be more extended. This may be attributed to the noise that leads to an underestimation of the sizes. It is important to note that the derived radii of the sizes may be underestimated,

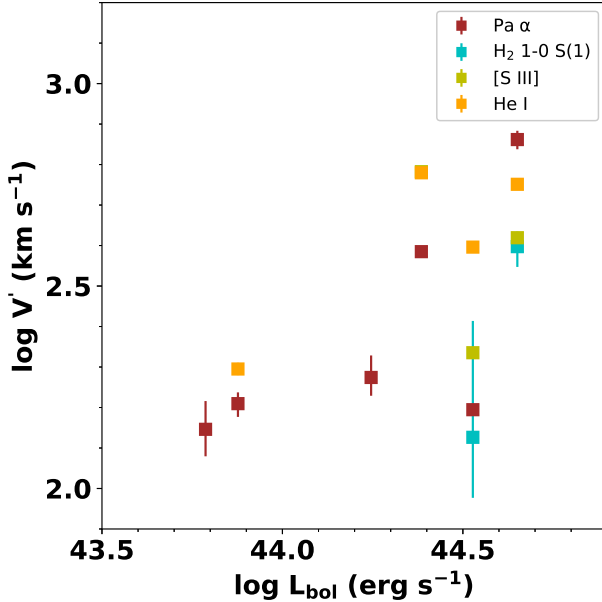


Figure 8. Maximum outflow velocity estimated from different emission lines as a function of bolometric luminosity.

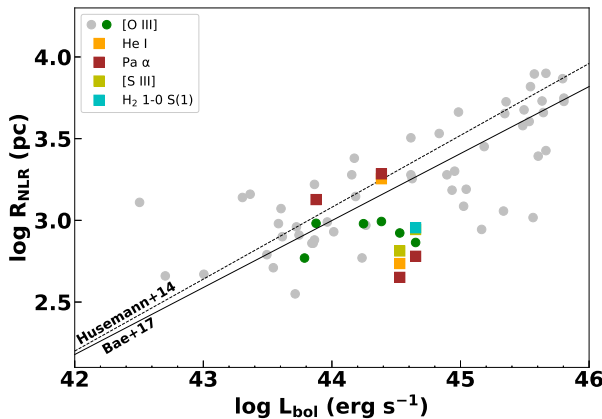


Figure 9. NLR size based on different emission lines as a function of bolometric luminosity. The dots show the measured sizes based on optical [O III] of the collected samples from Husemann et al. (2013), Husemann et al. (2014), Karouzos et al. (2016) and Bae et al. (2017). The colors mark the targets of our sample. Dashed and solid lines present the slope values from the linear regression of Husemann et al. (2014) and Bae et al. (2017), respectively.

as the low-surface-brightness component submerged by the noise was not considered in our adopted methodology (Speranza et al. 2022, 2024). Therefore, our reported R_{NLR} , as well as R_{out} , should be considered as conservative estimates or lower limits of the true physical extent of the ionized gas outflows.

4.3. AGN Strength and Outflow Properties

To characterize outflow sizes, Karouzos et al. (2016) estimated the radius encompassing half of the total broad [O III] emission flux as the effective radius r_{eff} . In the case of ID 2 in our sample, the radius of the bulk of the ionized outflow is $0.66^{+0.02}_{-0.02}$ kpc, which is similar to the effective radius of 0.60 kpc estimated from [O III] by Karouzos et al. (2016).

Generally, warm molecular outflows are anticipated to have a larger radius compared to the ionized outflows (Karouzos et al. 2016). This is because the warm molecular component of the outflow originates from the cooling of gas confined within the outflow. As shown in Table 3, the size of the warm molecular outflow ($0.87^{+0.20}_{-0.20}$ kpc) is larger than that of the ionized gas, although the difference is only at the level of one to two standard deviations. This may be attributed to the limited S/N and the measurement neglecting the low-surface-brightness component, which can lead to non-detection of the weaker and colder molecular gas over a broader region, as discussed in Section 4.2.

Using an X-ray-selected sample, Riffel et al. (2023) found that mass outflow rates and warm molecular outflow power are positively correlated with the AGN bolometric luminosity. As shown in Figure 10, we compare our only detected warm molecular outflow, tracing by H_2 1-0 S(1) of ID 2, with values from the literature (Riffel et al. 2023). We employ linear regression to illustrate the positive correlation among these values, and our results are generally consistent with the overall trend, albeit being slightly higher. It should be noted that the outflow energetics derived in this work are influenced by the analysis methods. First, as discussed in Section 4.2, R_{out} is likely underestimated, which leads to an overestimation of \dot{M}_{out} and \dot{E}_{out} . Second, as shown by Hervella Seoane et al. (2023), using maximum outflow velocities derived from parametric fits tends to produce higher estimates compared to other methods. In addition, the assumption of a constant density also affects the estimated properties of ionized outflows, since adopting lower densities would lead to an overestimation of the outflow mass and energy. These may contribute to the deviation from the result and the overall trend.

4.4. Spatially Resolved BPT Diagram

The Baldwin, Phillips, & Terlevich (BPT) diagram can be used to determine whether a spectrum is contributed from AGN or stellar components. Due to the difference in angular distance of 1 pixel between the red and blue cameras, we utilized the $[\text{N II}]/\text{H}\alpha$ line ratio fitted from the red 2D spectra using B-spline interpolation to estimate the $[\text{N II}]/\text{H}\alpha$ line ratio at the corresponding position in the blue 2D spectra of DBSP. Therefore, the

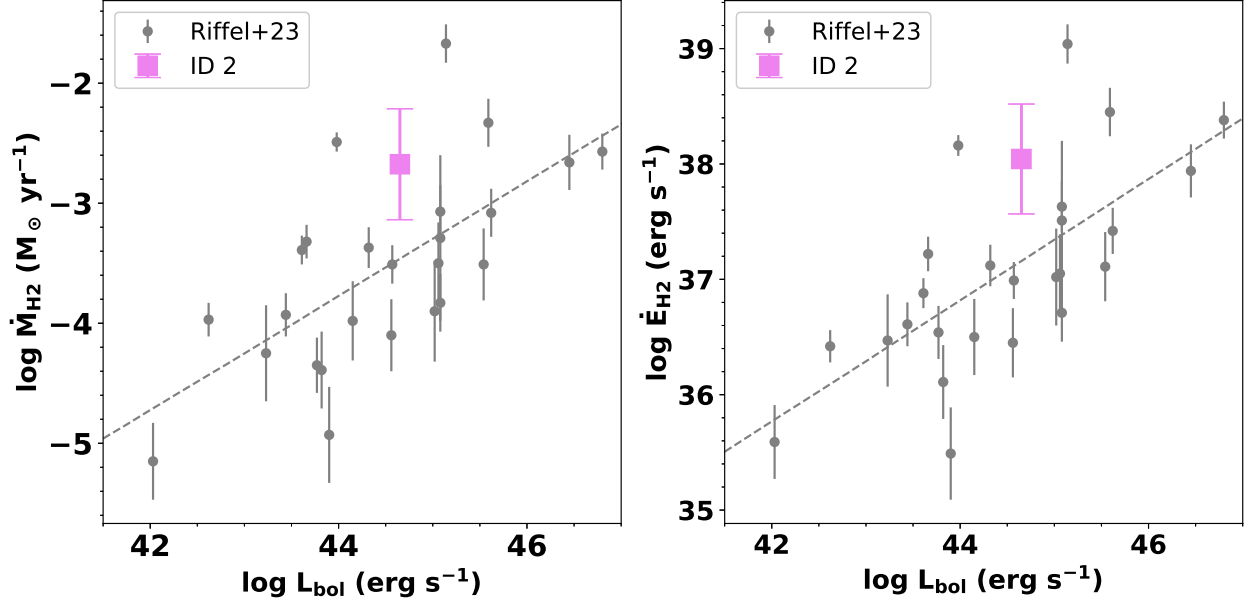


Figure 10. Left panel: plot of mass-outflow rates vs. AGN bolometric luminosity. Gray points are outflow properties obtained from Riffel et al. (2023). The dashed line shows a simple linear fit for the gray points. The violet square notes our results of H₂ 1-0 S(1) outflow of ID 2, under the same assumption of spherical geometry. Right panel: same as the left panel, but for the kinetic power of the H₂ outflow.

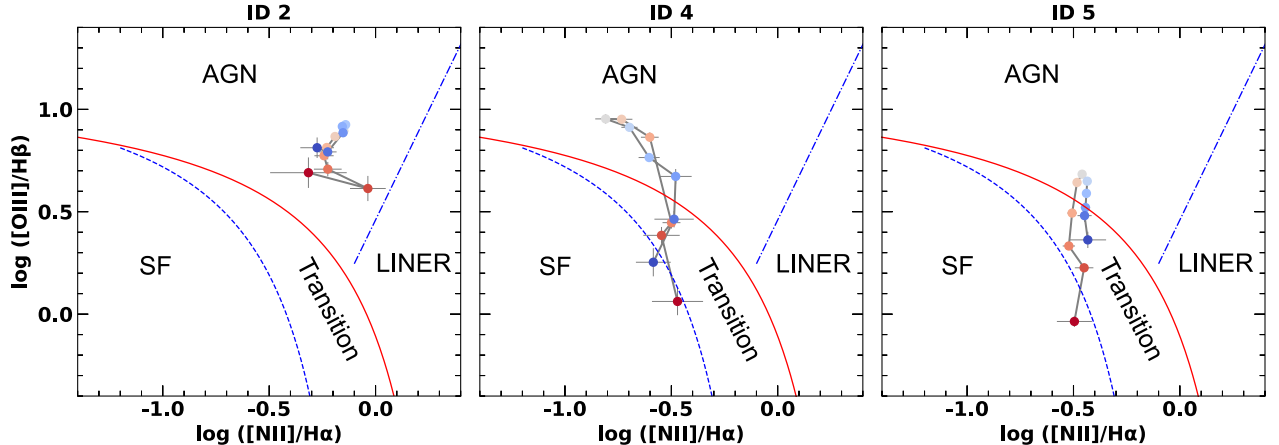


Figure 11. Spatially resolved BPT Diagram for ID 2, ID 4, and ID 5, respectively. The measurements are derived from the DBSP observations. Lighter colors indicate spectral pixels closer to the centers of the sources. The regions corresponding to AGN, star-forming (SF), transition, and Low-Ionization Nuclear Emission-line Regions (LINERs) are labeled. The spatial step between consecutive points is 0.389'', corresponding to 390, 352, and 471 pc for ID 2, ID 4, and ID 5, respectively.

spatial step between consecutive points is 0.389'', corresponding to 390, 352, and 471 pc for ID 2, ID 4, and ID 5, respectively.

Figure 11 illustrates the BPT diagrams for the three sources ID 2, ID 4, and ID 5, where lighter colors indicate spectral pixels closer to the center of the sources. We note that for ID 4 and ID 5, the spectra corresponding to several pixels in the center fall within the AGN region on the BPT diagram, and as we move farther

away from the center, they become closer to the region associated with stars. The spectra of ID 2 remain located in the AGN region at larger distances from the center, indicating that AGN photoionization or shock excitation continues to dominate the emission even in the outer regions, consistent with stronger AGN activity. This indicates that our two-dimensional spectrum possesses a specific spatial resolution capability and of-

fers a method for determining the regions affected by AGN activity.

4.5. Origin of Warm Molecular Gas Emission

The $H_2/Br\gamma$ line ratio serves as a useful tool for investigating the origin of H_2 emission. Riffel et al. (2021b) summarized that the H_2 emission can arise from three main excitation mechanisms: fluorescence ($H_2/Br\gamma < 0.4$), X-ray heating and shock-related excitation ($0.4 < H_2/Br\gamma < 6$), and the shock-dominated regime ($H_2/Br\gamma > 6$). We have detected the H_2 and $Br\gamma$ emission lines in ID 2, with an integrated $H_2/Br\gamma$ line ratio of approximately 1. This finding suggests that the H_2 emission is primarily driven by thermal processes in ID 2, including X-ray heating and shocks, possibly attributed to AGN activities.

4.6. Possibility of Detecting Both Ionized and Warm Molecular Outflows

Recent studies highlight the complex, multi-phase nature of AGN feedback. While ionized and cold molecular outflows are frequently detected in such systems (e.g., Rupke & Veilleux 2013; Ramos Almeida et al. 2022; Speranza et al. 2024), the warm molecular counterpart is not always observed (e.g., Ramos Almeida et al. 2017). And Riffel et al. (2023) found that the ionized outflow was found in 96% of their sample, while it was 76% for the warm molecular outflow. As in our sample, the occurrence of warm molecular outflows is notably lower at 16% (1 out of 6 objects having warm molecular outflows). We hypothesize that some potential outflow components might be submerged by noise due to the limited S/N, even for ID 2. Broad components in [O III] emission lines (see Figure A3) are evident. However, a similar profile is solely detected in $Pa\alpha$. Given the considerably higher S/N of [O III] emission compared to NIR lines, it is plausible that some outflow signatures are missed in this analysis. To address this problem, further high-quality and deep spectroscopic observations are needed. While we focus here on the ionized and warm molecular phase, a complete picture requires comparison with other gas phases (e.g., Speranza et al. 2022). Investigating the cold molecular gas phase through radio observations is also valuable for obtaining a more comprehensive understanding of AGN feedback. In addition, extensive work on type 1 AGNs is carried out in Qin et al. (2026, i.e., Paper-II).

5. SUMMARY

As a complement to Paper-I, we present a study focusing on comparing ionized and warm molecular gas outflows in six type-2 AGNs with redshifts below 0.1,

demonstrating extraordinary levels of ionized gas outflows. The study was conducted employing the TPSP and DBSP instruments on the P200 telescope and we supplement our data with archival SDSS data. We summarize the primary findings and crucial conclusions as follows.

1. The warm molecular gas traced by H_2 1-0 S(1) line is detected in two of six AGNs in our sample, with one (ID 2) showing significant outflow signatures. The non-detection of the outflow components in the remaining spectra may be due to the limited S/N. However, at least not all objects with strong ionized outflows have strong warm molecular outflows.
2. We estimate the radii of ionized and warm molecular outflow sizes for ID 2 to be $0.66^{+0.02}_{-0.02}$ kpc and $0.87^{+0.20}_{-0.20}$ kpc, respectively. The profile of H_2 is skewed to the left, indicating that the intensity distribution of the warm molecular outflow is different from the ionized outflow in ID 2.
3. A positive correlation between kinematics and luminosity is shown in both ionized and warm molecular lines, suggesting that more luminous AGNs, which reflect higher levels of AGN activity, tend to have a greater impact on the gas, probably driving the outflows.
4. We estimate the outflow rates of mass and energy of the warm molecular outflow of ID 2 and compare them with the X-ray-selected sample presented by Riffel et al. (2023). We find that ID 2 follows the expected positive correlation with the bolometric luminosity established by the comparison sample.
5. The spatially resolved BPT diagram of the three sources observed by DBSP suggests regions influenced by the AGN activities, providing a different way to measure the AGN strength, probably with a better resolution.
6. We find that the integrated $H_2/Br\gamma$ line ratio is approximately 1. This finding suggests that the H_2 emission is primarily driven by thermal processes in ID 2, including X-ray heating and shocks, possibly attributed to AGN activities.

¹ This work has been supported by the National Natural
² Science Foundation of China (NSFC-12473014, NSFC-
³ 12025303, NSFC-12203047), National Key R&D Pro-
⁴ gram of China No. 2022YFF0503401, 2023YFA1608100.
⁵ This research uses data obtained through the Tele-
⁶ scope Access Program (TAP), which has been funded by
⁷ the TAP member institutes (Proposal ID: CTAP2022-
⁸ A0037). We thank the DBSP observational data shared
⁹ by Luming Sun and Yibo Wang.

REFERENCES

Allington-Smith, J., Murray, G., Content, R., et al. 2002, PASP, 114, 892, doi: [10.1086/341712](https://doi.org/10.1086/341712)

Ayubinia, A., Xue, Y., Nguyen Le, H. A., et al. 2023, ApJ, 951, 7, doi: [10.3847/1538-4357/accf18](https://doi.org/10.3847/1538-4357/accf18)

Bae, H.-J., & Woo, J.-H. 2014, The Astrophysical Journal, 11

—. 2016, The Astrophysical Journal, 828, 97, doi: [10.3847/0004-637X/828/2/97](https://doi.org/10.3847/0004-637X/828/2/97)

Bae, H.-J., Woo, J.-H., Karouzos, M., et al. 2017, The Astrophysical Journal, 837, 91, doi: [10.3847/1538-4357/aa5f5c](https://doi.org/10.3847/1538-4357/aa5f5c)

Baldwin, J. A., Phillips, M. M., & Terlevich, R. 1981, PASP, 93, 5, doi: [10.1086/130766](https://doi.org/10.1086/130766)

Bessiere, P. S., & Ramos Almeida, C. 2022, MNRAS, 512, L54, doi: [10.1093/mnrasl/slac016](https://doi.org/10.1093/mnrasl/slac016)

Bianchin, M., Riffel, R. A., Storchi-Bergmann, T., et al. 2022, Monthly Notices of the Royal Astronomical Society, 510, 639, doi: [10.1093/mnras/stab3468](https://doi.org/10.1093/mnras/stab3468)

Caglar, T., Burtscher, L., Brandl, B., et al. 2020, Astronomy and Astrophysics, 634, A114, doi: [10.1051/0004-6361/201936321](https://doi.org/10.1051/0004-6361/201936321)

Calzetti, D. 1999, Ap&SS, 266, 243, doi: [10.1023/A:1002655227201](https://doi.org/10.1023/A:1002655227201)

Cappellari, M. 2022, Full spectrum fitting with photometry in ppxf: non-parametric star formation history, metallicity and the quenching boundary from 3200 LEGA-C galaxies at redshift $z \sim 0.8$, doi: [10.48550/arXiv.2208.14974](https://doi.org/10.48550/arXiv.2208.14974)

Carniani, S., Marconi, A., Maiolino, R., et al. 2016, A&A, 591, A28, doi: [10.1051/0004-6361/201528037](https://doi.org/10.1051/0004-6361/201528037)

Cresci, G., Marconi, A., Zibetti, S., et al. 2015a, A&A, 582, A63, doi: [10.1051/0004-6361/201526581](https://doi.org/10.1051/0004-6361/201526581)

Cresci, G., Mainieri, V., Brusa, M., et al. 2015b, ApJ, 799, 82, doi: [10.1088/0004-637X/799/1/82](https://doi.org/10.1088/0004-637X/799/1/82)

Davies, R., Baron, D., Shimizu, T., et al. 2020, MNRAS, 498, 4150, doi: [10.1093/mnras/staa2413](https://doi.org/10.1093/mnras/staa2413)

Fiore, F., Feruglio, C., Shankar, F., et al. 2017, A&A, 601, A143, doi: [10.1051/0004-6361/201629478](https://doi.org/10.1051/0004-6361/201629478)

González-Alfonso, E., Fischer, J., Spoon, H. W. W., et al. 2017, ApJ, 836, 11, doi: [10.3847/1538-4357/836/1/11](https://doi.org/10.3847/1538-4357/836/1/11)

Harrison, C. M., Costa, T., Tadhunter, C. N., et al. 2018, Nature Astronomy, 2, 198, doi: [10.1038/s41550-018-0403-6](https://doi.org/10.1038/s41550-018-0403-6)

Harrison, C. M., Alexander, D. M., Mullaney, J. R., et al. 2012, The Astrophysical Journal Letters, 760, L15, doi: [10.1088/2041-8205/760/1/L15](https://doi.org/10.1088/2041-8205/760/1/L15)

Heckman, T. M., Kauffmann, G., Brinchmann, J., et al. 2004, ApJ, 613, 109, doi: [10.1086/422872](https://doi.org/10.1086/422872)

Herter, T. L., Henderson, C. P., Wilson, J. C., et al. 2008, in Ground-based and Airborne Instrumentation for Astronomy II, Vol. 7014 (SPIE), 366–373, doi: [10.1117/12.789660](https://doi.org/10.1117/12.789660)

Hervella Seoane, K., Ramos Almeida, C., Acosta-Pulido, J. A., et al. 2023, A&A, 680, A71, doi: [10.1051/0004-6361/202347756](https://doi.org/10.1051/0004-6361/202347756)

Holden, L. R., Tadhunter, C. N., Morganti, R., & Oosterloo, T. 2023, MNRAS, 520, 1848, doi: [10.1093/mnras/stad123](https://doi.org/10.1093/mnras/stad123)

Husemann, B., Jahnke, K., Sánchez, S. F., et al. 2014, MNRAS, 443, 755, doi: [10.1093/mnras/stu1167](https://doi.org/10.1093/mnras/stu1167)

Husemann, B., Wisotzki, L., Sánchez, S. F., & Jahnke, K. 2013, A&A, 549, A43, doi: [10.1051/0004-6361/201220076](https://doi.org/10.1051/0004-6361/201220076)

Izotov, Y. I., & Thuan, T. X. 2016, Monthly Notices of the Royal Astronomical Society, 457, 64, doi: [10.1093/mnras/stv2957](https://doi.org/10.1093/mnras/stv2957)

Kaastra, J. S., & Bleeker, J. A. M. 2016, Astronomy & Astrophysics, 587, A151, doi: [10.1051/0004-6361/201527395](https://doi.org/10.1051/0004-6361/201527395)

Karouzos, M., Woo, J.-H., & Bae, H.-J. 2016, The Astrophysical Journal, 819, 148, doi: [10.3847/0004-637X/819/2/148](https://doi.org/10.3847/0004-637X/819/2/148)

Kormendy, J., & Ho, L. C. 2013, Annual Review of Astronomy and Astrophysics, 51, 511, doi: [10.1146/annurev-astro-082708-101811](https://doi.org/10.1146/annurev-astro-082708-101811)

Le, H. A. N., Pak, S., Jaffe, D. T., et al. 2015, *Advances in Space Research*, 55, 2509, doi: [10.1016/j.asr.2015.03.007](https://doi.org/10.1016/j.asr.2015.03.007)

Le, H. A. N., Qin, C., Xue, Y., et al. 2024, *The Astronomical Journal*

Le, H. A. N., Xue, Y., Lin, X., & Wang, Y. 2023, *ApJ*, 945, 59, doi: [10.3847/1538-4357/acb770](https://doi.org/10.3847/1538-4357/acb770)

Le, H. A. N., Woo, J.-H., Son, D., et al. 2017a, *The Astrophysical Journal*, 851, 8, doi: [10.3847/1538-4357/aa9656](https://doi.org/10.3847/1538-4357/aa9656)

Le, H. A. N., Pak, S., Kaplan, K. F., et al. 2017b, *The Astrophysical Journal*, 841, 13, doi: [10.3847/1538-4357/aa6bf7](https://doi.org/10.3847/1538-4357/aa6bf7)

Osterbrock, D. E., & Ferland, G. J. 2006, *Astrophysics of gaseous nebulae and active galactic nuclei*

Prochaska, J., Hennawi, J., Westfall, K., et al. 2020, *The Journal of Open Source Software*, 5, 2308, doi: [10.21105/joss.02308](https://doi.org/10.21105/joss.02308)

Pérez-Montero, E. 2017, *Publications of the Astronomical Society of the Pacific*, 129, 043001, doi: [10.1088/1538-3873/aa5abb](https://doi.org/10.1088/1538-3873/aa5abb)

Qin, C., Le, H. A. N., Xue, Y., et al. 2026, arXiv e-prints, arXiv:2601.10372, doi: [10.48550/arXiv.2601.10372](https://doi.org/10.48550/arXiv.2601.10372)

Ramasawmy, J., Stevens, J., Martin, G., & Geach, J. E. 2019, *Monthly Notices of the Royal Astronomical Society*, 486, 4320, doi: [10.1093/mnras/stz1093](https://doi.org/10.1093/mnras/stz1093)

Ramos Almeida, C., Piqueras López, J., Villar-Martín, M., & Bessiere, P. S. 2017, *Monthly Notices of the Royal Astronomical Society*, 470, 964, doi: [10.1093/mnras/stx1287](https://doi.org/10.1093/mnras/stx1287)

Ramos Almeida, C., Bischetti, M., García-Burillo, S., et al. 2022, *A&A*, 658, A155, doi: [10.1051/0004-6361/202141906](https://doi.org/10.1051/0004-6361/202141906)

Ramos Almeida, C., Acosta-Pulido, J. A., Tadhunter, C. N., et al. 2019, *Monthly Notices of the Royal Astronomical Society: Letters*, 487, L18, doi: [10.1093/mnrasl/slz072](https://doi.org/10.1093/mnrasl/slz072)

Rice, J. A. 2007, *Mathematical statistics and data analysis*, 3rd edn., Duxbury advanced series (Belmont, CA: Thomson/Brooks/Cole)

Riffel, R., Rodríguez-Ardila, A., Aleman, I., et al. 2013, *Monthly Notices of the Royal Astronomical Society*, 430, 2002, doi: [10.1093/mnras/stt026](https://doi.org/10.1093/mnras/stt026)

Riffel, R., Rodríguez-Ardila, A., & Pastoriza, M. G. 2006, *Astronomy & Astrophysics*, 457, 61, doi: [10.1051/0004-6361:20065291](https://doi.org/10.1051/0004-6361:20065291)

Riffel, R. A., Bianchin, M., Riffel, R., et al. 2021a, *Monthly Notices of the Royal Astronomical Society*, 503, 5161, doi: [10.1093/mnras/stab788](https://doi.org/10.1093/mnras/stab788)

Riffel, R. A., Vale, T. B., Storchi-Bergmann, T., & McGregor, P. J. 2014, *Monthly Notices of the Royal Astronomical Society*, 442, 656, doi: [10.1093/mnras/stu843](https://doi.org/10.1093/mnras/stu843)

Riffel, R. A., Zakamska, N. L., & Riffel, R. 2020, *Monthly Notices of the Royal Astronomical Society*, 491, 1518, doi: [10.1093/mnras/stz3137](https://doi.org/10.1093/mnras/stz3137)

Riffel, R. A., Storchi-Bergmann, T., Riffel, R., et al. 2021b, *Monthly Notices of the Royal Astronomical Society*, 504, 3265, doi: [10.1093/mnras/stab998](https://doi.org/10.1093/mnras/stab998)

—. 2023, *Monthly Notices of the Royal Astronomical Society*, 521, 1832, doi: [10.1093/mnras/stad599](https://doi.org/10.1093/mnras/stad599)

Rose, M., Tadhunter, C., Ramos Almeida, C., et al. 2018, *MNRAS*, 474, 128, doi: [10.1093/mnras/stx2590](https://doi.org/10.1093/mnras/stx2590)

Rose, M., Tadhunter, C., Ramos Almeida, C., et al. 2018, *Monthly Notices of the Royal Astronomical Society*, 474, 128, doi: [10.1093/mnras/stx2590](https://doi.org/10.1093/mnras/stx2590)

Rupke, D. S. N., & Veilleux, S. 2013, *The Astrophysical Journal*, 775, L15, doi: [10.1088/2041-8205/775/1/L15](https://doi.org/10.1088/2041-8205/775/1/L15)

Ruschel-Dutra, D., Storchi-Bergmann, T., Schnorr-Müller, A., et al. 2021, *Monthly Notices of the Royal Astronomical Society*, 507, 74, doi: [10.1093/mnras/stab2058](https://doi.org/10.1093/mnras/stab2058)

Schulze, A., Silverman, J. D., Daddi, E., et al. 2019, *Monthly Notices of the Royal Astronomical Society*, 488, 1180, doi: [10.1093/mnras/stz1746](https://doi.org/10.1093/mnras/stz1746)

Scoville, N. Z., Hall, D. N. B., Ridgway, S. T., & Kleinmann, S. G. 1982, *The Astrophysical Journal*, 253, 136, doi: [10.1086/159618](https://doi.org/10.1086/159618)

Sexton, R. O., Matzko, W., Darden, N., Canalizo, G., & Gorjian, V. 2020, *Monthly Notices of the Royal Astronomical Society*, 500, 2871, doi: [10.1093/mnras/staa3278](https://doi.org/10.1093/mnras/staa3278)

Speranza, G., Ramos Almeida, C., Acosta-Pulido, J. A., et al. 2022, *A&A*, 665, A55, doi: [10.1051/0004-6361/202243585](https://doi.org/10.1051/0004-6361/202243585)

—. 2024, *A&A*, 681, A63, doi: [10.1051/0004-6361/202347715](https://doi.org/10.1051/0004-6361/202347715)

Stanley, F., Harrison, C. M., Alexander, D. M., et al. 2015, *Monthly Notices of the Royal Astronomical Society*, 453, 591, doi: [10.1093/mnras/stv1678](https://doi.org/10.1093/mnras/stv1678)

Storchi-Bergmann, T., McGregor, P. J., Riffel, R. A., et al. 2009, *Monthly Notices of the Royal Astronomical Society*, 394, 1148, doi: [10.1111/j.1365-2966.2009.14388.x](https://doi.org/10.1111/j.1365-2966.2009.14388.x)

Storey, P. J., & Hummer, D. G. 1995, *MNRAS*, 272, 41, doi: [10.1093/mnras/272.1.41](https://doi.org/10.1093/mnras/272.1.41)

U, V., Medling, A., Sanders, D., et al. 2013, *The Astrophysical Journal*, 775, 115, doi: [10.1088/0004-637X/775/2/115](https://doi.org/10.1088/0004-637X/775/2/115)

Vazdekis, A., Koleva, M., Ricciardelli, E., Röck, B., & Falcón-Barroso, J. 2016, Monthly Notices of the Royal Astronomical Society, 463, 3409, doi: [10.1093/mnras/stw2231](https://doi.org/10.1093/mnras/stw2231)

Virtanen, P., Gommers, R., Oliphant, T. E., et al. 2020, Nature Methods, 17, 261, doi: [10.1038/s41592-019-0686-2](https://doi.org/10.1038/s41592-019-0686-2)

Woo, J.-H., Bae, H.-J., Son, D., & Karouzos, M. 2016, The Astrophysical Journal, 817, 108, doi: [10.3847/0004-637X/817/2/108](https://doi.org/10.3847/0004-637X/817/2/108)

Xue, Y. 2017, New Astronomy Reviews, 79, 59, doi: [10.1016/j.newar.2017.09.002](https://doi.org/10.1016/j.newar.2017.09.002)

Zhang, K., Dong, X.-B., Wang, T.-G., & Gaskell, C. M. 2011, ApJ, 737, 71, doi: [10.1088/0004-637X/737/2/71](https://doi.org/10.1088/0004-637X/737/2/71)

Zubovas, K., & King, A. R. 2014, Monthly Notices of the Royal Astronomical Society, 439, 400, doi: [10.1093/mnras/stt2472](https://doi.org/10.1093/mnras/stt2472)

APPENDIX

A. SPECTRA FOR INDIVIDUAL SOURCES

The NIR spectra of TPSP for our 6 targets are shown in Figure A1. The emission lines that are significant enough are marked. ID 2 shows the most and the strongest emission lines with the highest S/N, which can be seen in Table 2.

In Figure A2, we present the 1D DBSP (SDSS) spectra for ID 2, ID 4, and ID 5 (ID 1, ID 3, and ID 6), respectively, showcasing the original spectra (black line), the stellar component (red lines), and the pure emission line component (blue line), and highlighting some important emission lines (gray dashed vertical lines) present in both the blue and red observed spectra simultaneously. An absorption structure spanning from 6600 to 6900 Å in the observed frame is noticeable. Importantly, these structures remain consistent across different redshifts, suggesting that they likely arise from dusty clouds within the Milky Way.

The electron density n_e and electron temperature T_e are derived from the flux ratios of the forbidden lines. We employ the [S II] doublet ratio $F(6716 \text{ \AA})/F(6731 \text{ \AA})$ to diagnose the electron density, following Equation (16) in Pérez-Montero (2017). Since the [O II] doublet (3726 Å and 3729 Å) is not resolved in our data, and the [O III] lines have a higher S/N that allows for a more reliable temperature diagnostic, we estimate the electron temperature using the [O III] ratio $(F(4959 \text{ \AA}) + F(5007 \text{ \AA}))/F(4363 \text{ \AA})$, following Equation (8) in Pérez-Montero (2017). The results estimated from SDSS and DBSP spectra are listed in Table A1. Although trans-auroral lines have been shown to trace denser gas phases and provide more realistic outflow parameters (Rose et al. 2018; Davies et al. 2020; Holden et al. 2023; Speranza et al. 2024), these lines are too weak to be detected in our current data. Thus, we utilize the [S II] doublet to constrain the density. While this may still underestimate the density, it still provides a more accurate estimate than assuming a fixed value. In the main text, we use the electron density estimates derived from the SDSS spectra for all six targets to ensure consistency.

We compare the normalized model profiles of optical [O III] and NIR emission lines in Figure A3. The outflow component of H₂ 1-0 S(1) seems close to the centroid of the profile of [O III], indicating the same origin of the outflows.

Table A1. Electron Temperature and Density from SDSS and DBSP

ID	SDSS		DBSP	
	T_e (K)	n_e (cm ⁻³)	T_e (K)	n_e (cm ⁻³)
1	19855.70	1278.02	—	—
2	11751.64	431.37	10568.85	357.03
3	16019.36	29.04	—	—
4	25506.18	82.11	21844.95	180.53
5	10634.59	235.18	9649.51	363.61
6	20161.93	41.51	—	—

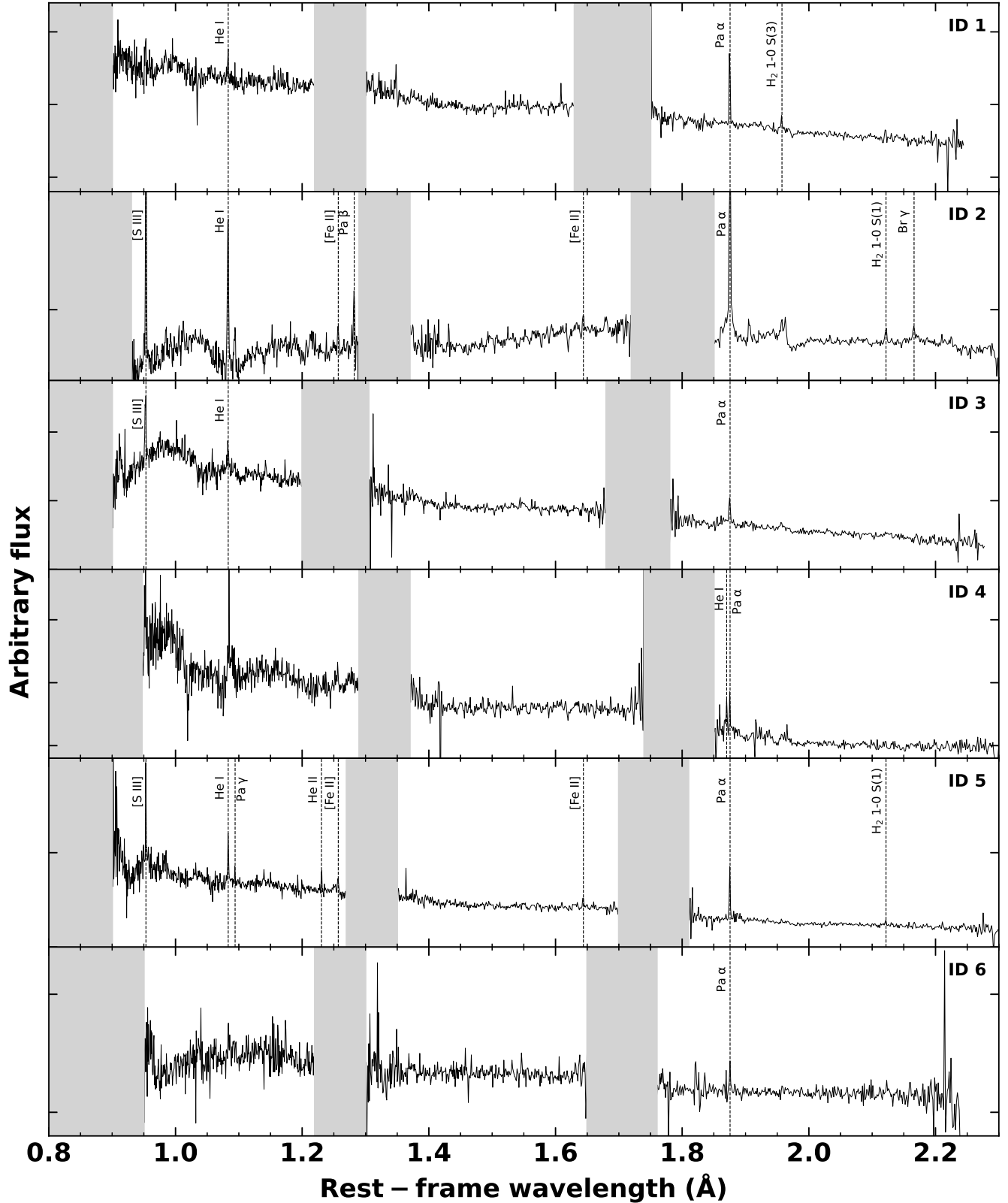


Figure A1. TPSP NIR spectra of the AGNs. The spectra have been corrected by the redshifts concerning the stellar absorption line from the optical spectral analysis of SDSS. The blocked areas indicate the wavelength ranges largely influenced by the sky lines. The emission lines that are significant enough are marked by the dotted lines.

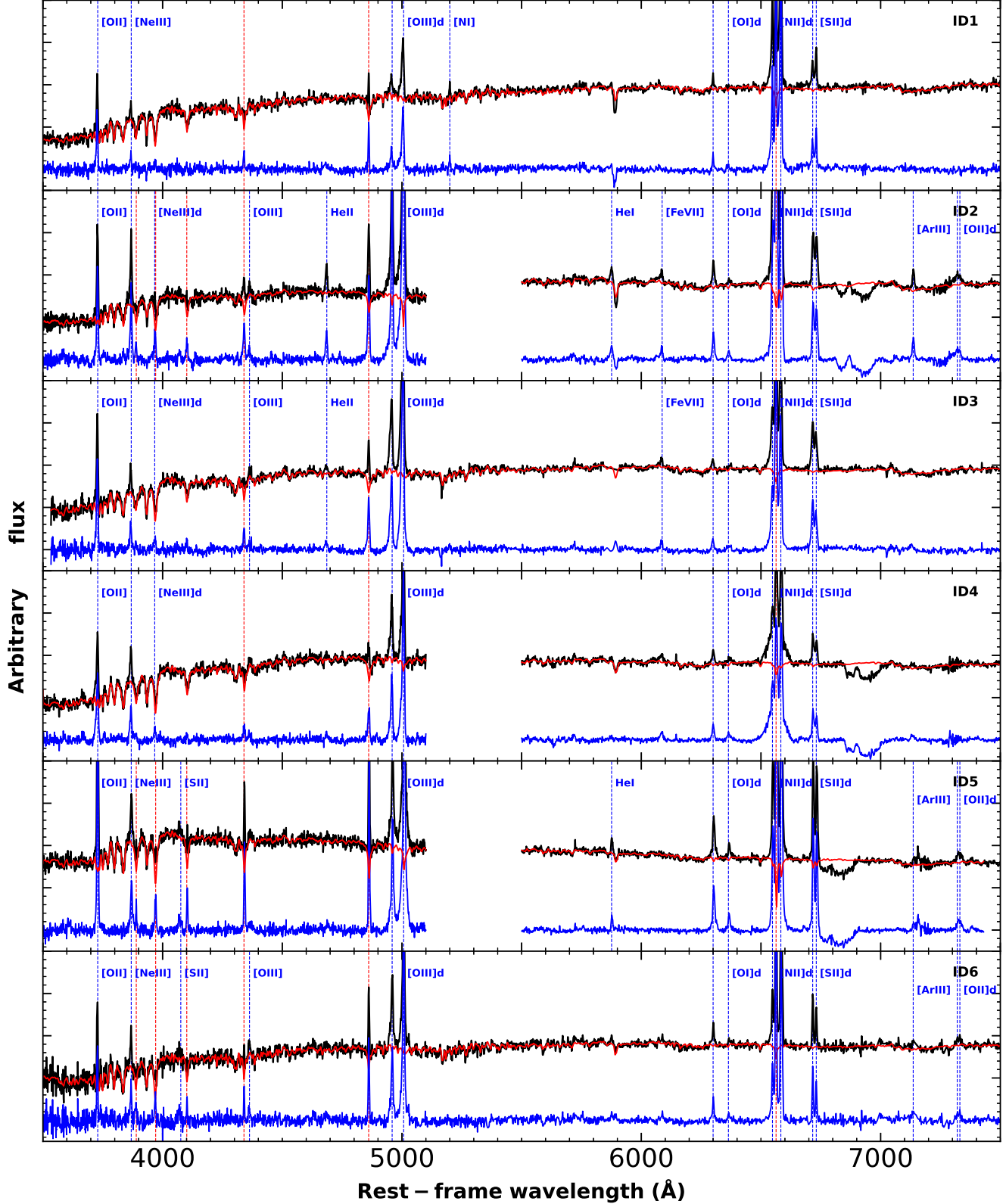


Figure A2. DBSP and SDSS optical spectra of the AGNs (black). The spectra have been corrected concerning the stellar absorption line. The best-fit stellar population models are plotted in red, and the residual emission line spectra are in blue. H β , [O III], H α + [N II] and the absorption structure range 6600–6900 Å are masked when running pPXF, to make sure that a single Gaussian model is reliable to fit an emission line. The dashed lines indicate the wavelengths of some important emission lines in vacuum.

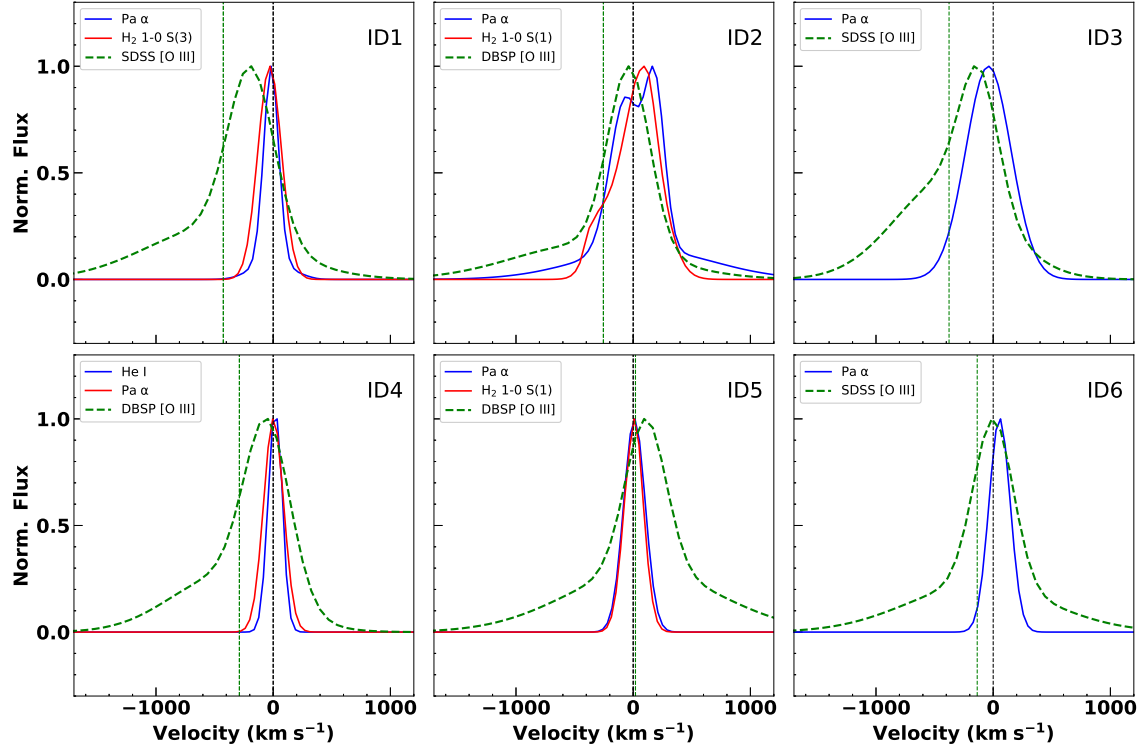


Figure A3. A comparison between optical [O III] line profile (green) and NIR emission lines. The fluxes have been normalized by the peak values of the fitted Gaussian profiles. The dotted lines mark the centroid of the profile fitted by the Gaussian components, and the black dashed lines note 0 values.